

**REPUBLIC OF TURKEY**  
**YILDIZ TECHNICAL UNIVERSITY**  
**GRADUATE SCHOOL OF NATURAL AND APPLIED SCIENCES**

**TWO DIMENSIONAL COMPUTATIONAL ANALYSIS OF  
FLOW INDUCED VIBRATIONS**



**Asim Ozan MUTLU**

MASTER OF SCIENCE THESIS

Department of Mechanical Engineering

Machine Theory and Control

Advisor

Asst. Prof. Meral BAYRAKTAR PhD

Co-Advisor

Assoc. Prof. Seyfettin BAYRAKTAR PhD

July 2019

**REPUBLIC OF TURKEY**  
**YILDIZ TECHNICAL UNIVERSITY**  
**GRADUATE SCHOOL OF NATURAL AND APPLIED SCIENCES**

**TWO DIMENSIONAL COMPUTATIONAL ANALYSIS OF FLOW  
INDUCED VIBRATIONS**

A thesis submitted by Asım Ozan MUTLU in partial fulfillment of the requirements for the degree of MASTER OF SCIENCE is approved by the committee on 05.07.2019 in Department of Mechanical Engineering, Machine Theory and Control Program.

Asst. Prof. Meral BAYRAKTAR PhD

Assoc. Prof. Seyfettin BAYRAKTAR PhD

Yıldız Technical University

Yıldız Technical University

Advisor

Co-Advisor

**Approved by the Examining Committee**

Asst. Prof. Meral BAYRAKTAR PhD, Advisor

Yıldız Technical University

\_\_\_\_\_

Assoc. Prof. Seyfettin BAYRAKTAR PhD, Co-Advisor

Yıldız Technical University

\_\_\_\_\_

Prof. Hakan DEMİR PhD, Member

Yıldız Technical University

\_\_\_\_\_

Assoc. Prof. Ömer Kemal KINACI PhD, Member

Istanbul Technical University

\_\_\_\_\_

I hereby declare that I have obtained the required legal permissions during data collection and exploitation procedures, that I have made the in-text citations and cited the references properly, that I have not falsified and/or fabricated research data and results of the study and that I have abided by the principles of the scientific research and ethics during my Thesis Study under the title of TWO DIMENSIONAL COMPUTATIONAL ANALYSIS OF FLOW INDUCED VIBRATIONS by my supervisors, Asst. Prof. Meral BAYRAKTAR PhD and Assoc. Prof. Seyfettin BAYRAKTAR PhD. In the case of a discovery of false statement, I am to acknowledge any legal consequence.

Asım Ozan MUTLU

Signature

*Dedicated to my mother and father*



## ACKNOWLEDGEMENTS

---

I would like to thank my supervisors Asst. Prof. Meral BAYRAKTAR PhD and Assoc. Prof. Seyfettin BAYRAKTAR PhD for their support and guidance for this work.

I would also like to thank to all my friends for their love, support and cheer me up whenever I need.

Last but not least, thanks to my mother and father for their endless love, support and encouragement throughout my whole life. Thanks to them, I am who I am today.

Asım Ozan MUTLU



# TABLE OF CONTENTS

---

LIST OF SYMBOLS .....	IX
LIST OF ABBREVIATIONS.....	XII
LIST OF FIGURES .....	13
LIST OF TABLES .....	15
ABSTRACT.....	XVI
ÖZET .....	XVIII
1 Introduction .....	1
1.1 Literature Review .....	1
1.2 Objective of the Thesis .....	4
1.3 Hypothesis.....	4
2 Theoretical Background of Vortex-Induced Vibration.....	5
2.1 Regime of Flow.....	5
2.2 Vortex Shedding .....	5
2.3 Lift and Drag Forces.....	7
2.4 Vortex-Induced Vibration.....	7
2.5 Vortex Patterns .....	8
2.6 Dynamics of 1DOF System.....	9
2.7 Effect of Mass Ratio.....	11
2.8 Effect of Aspect Ratio .....	13
3 Computational Fluid Dynamics.....	15
3.1 Introduction.....	15
3.2 Fundamentals of Fluid Dynamics.....	15

3.2.1	Conservation of Mass .....	15
3.2.2	Conservation of Momentum .....	16
3.3	CFD Methodology.....	16
3.4	Turbulence Modelling.....	17
3.4.1	SST k- $\omega$ Turbulence Model.....	17
3.4.2	Near Wall Boundary Layer .....	19
3.5	Pressure – Velocity Coupling.....	19
3.6	Discretization Schemes .....	20
3.6.1	Spatial Discretization .....	20
3.6.2	Temporal Discretization.....	21
3.7	Dynamic Mesh Methods.....	22
4	Numerical Simulation Setup.....	23
4.1	Solution Domain and Mesh Generation.....	23
4.2	Mesh Independence Study.....	24
4.3	Validation of 1DOF VIV Simulation .....	26
4.3.1	Simulation Setup .....	26
4.3.2	Results .....	27
5	1DOF Vortex-Induced Vibration with Different Damping Parameters .....	39
5.1	Numerical Setup .....	39
5.2	Results for $\zeta = 0.028$ .....	40
5.2.1	Amplitude Ratio.....	40
5.2.2	Drag and Lift Coefficients.....	42
5.2.3	Frequency Ratio and Phase Angle.....	46
5.2.4	Vortex formation modes.....	50
5.3	Results for $\zeta = 0.074$ .....	51
5.3.1	Amplitude Ratio.....	51

5.3.2	Drag and Lift Coefficients.....	52
5.3.3	Frequency Ratio and Phase Angle.....	57
5.3.4	Vortex Formation Modes.....	61
6	Conclusion.....	63
6.1	Conclusion.....	63
6.2	Future work suggestions.....	63
A	6DOF Solver UDF Code .....	65
	References.....	66
	Publications from the thesis.....	69

## LIST OF SYMBOLS

---

$A$	Displacement Amplitude of Cylinder
$A_s$	Aspect Ratio
$A^*$	Dimensionless Amplitude
$c$	Damping of Structure
$C$	Courant Number
$C_A$	Potential Added Mass Coefficient
$C_{EA}$	Effective Added Mass Coefficient
$C_L$	Lift Coefficient
$C_D$	Drag Coefficient
$D$	Cylinder Diameter
$f$	Body Oscillation Frequency
$F_0$	Maximum Fluid Force Exerted on Cylinder
$F_D$	Drag Force
$F_L$	Lift Force
$f_n$	Natural Frequency of System in Water
$f_v$	Vortex Shedding Frequency
$F_y$	Fluid Forces Exerted on Cylinder
$f^*$	Frequency Ratio
$g$	Gravity
$G_k$	Generation of the Turbulence Kinetic Energy
$G\omega$	Generation of the Specific Dissipation Rate
$k$	Turbulent Kinetic Energy
$k_s$	Stiffness of Structure

L	Cylinder Length
m	Mass of Cylinder
$m_A$	Added Mass
$m_d$	Displaced Fluid Mass
$m^*$	Mass Ratio
$m^*\zeta$	Mass-damping Parameter
p	Pressure
P	Pair of Vortices Per Cycle
Re	Reynolds Number
S	Single Vortices Per Cycle
$S_k$	User-Defined Source Terms for the Turbulence Kinetic Energy
$S_\omega$	User-Defined Source Terms for the Specific Dissipation Rate
St	Strouhal Number
t	Time
$T_v$	Vortex Shedding Period
U	Free Stream Velocity
$U_r$	Reduced Velocity
$U_\tau$	Friction Velocity Near the Wall
$\vec{u}$	Velocity Vector
$\vec{u}(u, v, w)$	Velocity Vector with respect to u, v and w (x, y and z respectively) Direction Components
$u^+$	Dimensionless Velocity
y	Transverse Direction in y Coordinate
$y_f$	First Cell height
$y^+$	Dimensionless First Cell Height
$\zeta$	Damping Ratio

$\lambda$	Wavelength of Cylinder
$\lambda^*$	Wavelength Ratio
$\rho$	Fluid Density
$\Delta t$	Time Step Size
$\Delta x$	Mesh Size in x Direction
$\mu$	Dynamic Viscosity
$\mu_t$	Turbulent Viscosity
$\sigma_k$	Turbulent Prandtl Number for the Turbulence Kinetic Energy
$\sigma_\omega$	Turbulent Prandtl Number for the Specific Dissipation Rate
$\Gamma_k$	Effective Diffusivity of the Turbulent Kinetic Energy
$\Gamma_\omega$	Effective Diffusivity of the Specific Dissipation Rate
$\nabla$	Gradient
$\omega$	The Specific Dissipation Rate
$\omega_d$	Angular Frequency of Cylinder Displacement
$\omega_n$	Angular Natural Frequency of System in Water
$\phi$	Phase Angle
$\nu$	Kinematic viscosity.

## LIST OF ABBREVIATIONS

---

CFD	Computational Fluid Dynamics
DOF	Degree of Freedom
FVM	Finite Volume Method
FSM	Fractional Step Method
NITA	Non-Iterative Time Advancement
PISO	Pressure-Implicit with Splitting of Operators
RNG	Re-Normalization Group
QUICK	Quadratic Upstream Interpolation for Convective Kinematics
SIMPLE	Semi-Implicit Method for Pressure-Linked Equations
SIMPLEC	SIMPLE – Consistent
SST k- $\omega$	Shear Stress Transport k- $\omega$ Turbulence Model
UDF	User Defined Function
URANS	Unsteady Reynolds Averaged Navier Stokes
VIV	Vortex-Induced Vibration

## LIST OF FIGURES

<b>Figure 2.1</b>	Schematics of physical model .....	8
<b>Figure 2.2</b>	Map of vortex pattern as a function of dimensionless amplitude and wave length ratio (Williamson and Roshko, 1988) .....	9
<b>Figure 2.3</b>	Frequency ratio, $f^*=f/f_n$ , in air (a) and water (b) as a function of $Ur$ (Sumer and Fredsøe, 1997).....	13
<b>Figure 2.4</b>	Dimensionless amplitude, $A^*$ , as a function of $Ur$ of different mass ratios ( $m^*=10.1$ Kahalak and Williamson, 1999, $m^*=248$ Feng, 1968) .....	13
<b>Figure 2.5</b>	Dimensionless amplitude, $A^*=A/D$ , as a function of $Ur$ with different aspect ratios (Rahman and Thiagarajan, 2015) .....	14
<b>Figure 3.1</b>	Types of flows and suggested $y^+$ values. (Anderson, 1995) .....	19
<b>Figure 3.2</b>	Overview of iterative segregated pressure-based solver (ANSYS Fluent Theory Guide, 2019) .....	21
<b>Figure 4.1</b>	Solution domain.....	23
<b>Figure 4.2</b>	Mesh structure applied to the computational domain .....	24
<b>Figure 4.3</b>	Mesh structure applied to the cylinder .....	24
<b>Figure 4.4</b>	Amplitude ratio, $A^*$ , as a function of reduced velocity, $Ur$ .....	28
<b>Figure 4.5</b>	Time trace of $A^*$ , $C_L$ and $C_D$ for a) $Ur=3$ and b) $Ur=4$ .....	29
<b>Figure 4.6</b>	Time trace of $A^*$ , $C_L$ and $C_D$ for c) $Ur=5$ , d) $Ur=6$ and e) $Ur=7$ .....	30
<b>Figure 4.7</b>	Time trace of $A^*$ , $C_L$ and $C_D$ for f) $Ur=8$ , g) $Ur=9$ and h) $Ur=10$ .....	31
<b>Figure 4.8</b>	Time trace of $A^*$ , $C_L$ and $C_D$ for i) $Ur=11$ , j) $Ur=12$ and k) $Ur=13$ .....	32
<b>Figure 4.9</b>	Summary of force coefficients in terms of $C_D$ max, $C_D$ mean, $C_L$ max and $C_L$ rms as function of corresponding $Ur$ .....	33
<b>Figure 4.10</b>	Frequency ratio $f^*$ as a function of corresponding $Ur$ .....	34
<b>Figure 4.11</b>	Spectral density of displacement of corresponding $Ur$ .....	35
<b>Figure 4.12</b>	Spectral density of displacement of corresponding $Ur$ .....	36
<b>Figure 4.13</b>	Phase angle, $\phi$ , as a function of corresponding $Ur$ .....	37
<b>Figure 4.14</b>	Vortex modes of $Ur=4$ (2S), $Ur=5$ (2P) and $Ur=8$ (2P) .....	38
<b>Figure 5.1</b>	Amplitude ratio, $A^*$ , as a function of reduced velocity $Ur$ for $\zeta=0.028$ .....	41
<b>Figure 5.2</b>	Time trace of $A^*$ , $C_L$ and $C_D$ for a) $Ur=3.6$ for $\zeta=0.028$ .....	42

<b>Figure 5.3</b>	Time trace of $A^*$ , $C_L$ and $C_D$ for b) $Ur=4$ , c) $Ur=5$ and d) $Ur=6$ for $\zeta=0.028$ .....	43
<b>Figure 5.4</b>	Time trace of $A^*$ , $C_L$ and $C_D$ for e) $Ur=7$ , f) $Ur=8$ and g) $Ur=9$ for $\zeta=0.028$ .....	44
<b>Figure 5.5</b>	Time trace of $A^*$ , $C_L$ and $C_D$ for h) $Ur=10$ , i) $Ur=11$ and j) $Ur=12$ for $\zeta=0.028$ .....	45
<b>Figure 5.6</b>	Summary of force coefficients in terms of $C_D$ max, $C_D$ mean, $C_L$ max and $C_L$ rms as function of corresponding $Ur$ for $\zeta=0.028$ .....	46
<b>Figure 5.7</b>	Frequency ratio $f^*$ as a function of corresponding $Ur$ for $\zeta=0.028$ .....	47
<b>Figure 5.8</b>	Spectral density of displacement of corresponding $Ur$ for $\zeta=0.028$ .....	48
<b>Figure 5.9</b>	Spectral density of displacement of corresponding $Ur$ for $\zeta=0.028$ .....	49
<b>Figure 5.10</b>	Phase angle, $\phi$ , as a function of corresponding $Ur$ for $\zeta=0.028$ .....	50
<b>Figure 5.11</b>	Vortex modes of $Ur=4$ (2S), $Ur=5$ (2P) and $Ur=8$ (2P) for $\zeta=0.028$ .....	51
<b>Figure 5.12</b>	Amplitude ratio, $A^*$ , as a function of reduced velocity $Ur$ for $\zeta=0.074$ .....	52
<b>Figure 5.13</b>	Time trace of $A^*$ , $C_L$ and $C_D$ for a) $Ur=3.6$ and b) $Ur=4$ for $\zeta=0.074$ .....	53
<b>Figure 5.14</b>	Time trace of $A^*$ , $C_L$ and $C_D$ for c) $Ur=5$ , d) $Ur=6$ and e) $Ur=7$ for $\zeta=0.074$ .....	54
<b>Figure 5.15</b>	Time trace of $A^*$ , $C_L$ and $C_D$ for f) $Ur=8$ , g) $Ur=9$ and h) $Ur=10$ for $\zeta=0.074$ .....	55
<b>Figure 5.16</b>	Time trace of $A^*$ , $C_L$ and $C_D$ for i) $Ur=11$ and j) $Ur=12$ for $\zeta=0.074$ .....	56
<b>Figure 5.17</b>	Summary of force coefficients in terms of $C_D$ max, $C_D$ mean, $C_L$ max and $C_L$ rms as function of corresponding $Ur$ for $\zeta=0.074$ .....	57
<b>Figure 5.18</b>	Frequency ratio $f^*$ as a function of corresponding $Ur$ for $\zeta=0.074$ .....	58
<b>Figure 5.19</b>	Spectral density of displacement of corresponding $Ur$ for $\zeta=0.074$ .....	59
<b>Figure 5.20</b>	Spectral density of displacement of corresponding $Ur$ for $\zeta=0.074$ .....	60
<b>Figure 5.21</b>	Phase angle, $\phi$ , as a function of corresponding $Ur$ for $\zeta=0.074$ .....	61
<b>Figure 5.22</b>	Vortex modes of $Ur=5$ (2S), $Ur=6$ (2P) and $Ur=8$ (2P) for $\zeta=0.074$ .....	62

## LIST OF TABLES

---

<b>Table 2.1</b> Regimes of flow around a cylindrical structure in steady flow (Sumer & Fredsøe, 1997).....	6
<b>Table 2.2</b> Dimensionless Parameters.....	12
<b>Table 4.1</b> Comparison of different grid size.....	25
<b>Table 4.2</b> Simulation parameters for validation.....	27
<b>Table 5.1</b> Simulation parameters for $\zeta = 0.028$ and $\zeta = 0.074$ .....	40



## TWO DIMENSIONAL COMPUTATIONAL ANALYSIS OF FLOW INDUCED VIBRATIONS

Asım Ozan MUTLU

Department of Mechanical Engineering  
Machine Theory and Control Department  
Master of Science Thesis

Advisor: Asst. Prof. Meral BAYRAKTAR PhD

Co-advisor: Assoc. Prof. Seyfettin BAYRAKTAR PhD

One of the difficult challenges that engineers encounter nowadays is the Vortex Induced Vibration (VIV). VIV occurs when a bluff body is subjected to external fluid flow. Vortices shed from the structures cause bluff bodies to oscillate. This oscillation can lead to failures of the structures. With the recent development of computer technologies, VIV have been caught attention by many researchers. Although, extensive research has been done until now, there are still research areas to be investigated on VIV.

In this study, one of the most important parameters of VIV, which is damping of the structure, is investigated and the results are compared with the experimental study of the previous research. The simulations are done with 2D cylindrical cross-section structure that is free to move in transverse direction. Overall, the general trend is well captured, however due to 2D limitations some results are not consistent with

experimental data. The results are shown and overall, it is concluded that the response of the amplitude decreases with the increased damping of the structure and a shift occurs in the beginning of the lock-in region with increasing damping.

**Keywords:** Computational fluid dynamics, vortex-Induced vibration, URANS method, damping



# İKİ BOYUTLU AKIŞA BAĞLI TİTREŞİMLERİN SAYISAL ANALİZİ

Asım Ozan MUTLU

Makine Mühendisliği Ana Bilim Dalı

Makine Teorisi ve Kontrol Bölümü

Yüksek Lisans Tezi

Danışman: Dr. Öğr. Üyesi Meral Bayraktar

Eş-Danışman: Doç. Dr. Seyfettin Bayraktar

Günümüzde mühendislerin karşılaştığı en zorlu problemlerden biri girdap kaynaklı titreşim problemidir. Girdap kaynaklı titreşimler, bir yapının maruz kaldığı akış sonucunda oluşan girdaplardan dolayı meydana gelir. Bu girdaplar periyodik hale gelerek yapının salınım yapmasına sebep olur. Bu olguya, girdap kaynaklı titreşim denmektedir. Bu salınım, yapıların bozulmasına neden ve ciddi hasarlar almasına sebep olabilir. Günümüzde bilgisayar teknolojilerindeki son gelişmeler sayesinde, girdap kaynaklı titreşimler, birçok araştırmacı tarafından incelenmeye başlanmıştır. Şimdiye kadar kapsamlı araştırmalar yapılmış olmasına rağmen, hala bu konuda geniş çapta araştırılacak yönler bulunmaktadır.

Bu çalışmada, girdap kaynaklı titreşimlerin en önemli parametresinden birisi olan sönümlenme parametresi incelenmiş ve sonuçlar önceki daha önceden yapılmış deneysel bir çalışma ile karşılaştırılmıştır. Simülasyonlar, tek serbestlik derecesinden akış yönüne dik hareket edebilen, silindirik bir yapıda

gerçekleştirilmiştir. Yapılan simülasyonlarda; genel olarak, deneysel sonuçlarla aynı davranış yakalansada, simülasyonlar iki boyutlu alanda gerçekleştirildiğinden dolayı bazı sonuçlarda tutarsızlık gözlemlenmiştir. Birimsiz deplasman, frekans oranı, girdap modları ve faz açısı sonuçları gösterilmiş, genel olarak şu sonuca ulaşılmıştır; sönümlenme artırıldığında genliğin azaldığı ve senkronize bölgeye geçişte bir ertelenme olduğu gözlemlenmiştir. Aynı sonuçlar karşılaştırılan deneysel çalışmada da gözlemlenmiştir.

**Anahtar Kelimeler:** Hesaplamalı akışkanlar dinamiği, girdap kaynaklı titreşimler, URANS metodu, sönümlenme



### 1.1 Literature Review

It is known to mankind that engineering has an important role to find innovative solutions to real life problems. These challenging encounters force engineering disciplines to constantly find different and innovative approaches. One of these challenges that engineering encounters is the Flow-Induced Vibration also known as Vortex-Induced Vibration (VIV).

VIV occurs when a bluff body is subjected to an external fluid flow. Vortices shed from the structures causes bluff bodies to oscillate. This oscillation can lead to failure of the structures and it can be even catastrophic like Tacoma Bridge, USA, 1940. VIV can occur in many engineering applications such as; coastal and marine structures like offshore platforms, aerostructures like airfoils, heat exchangers, bridges and so on.

Until now, VIV has been studied extensively by many researches with different aspects; with different structural parameters to different geometric properties. One can see the reviews by Khalak and Williamson (Khalak and Williamson, 1999) Sarpkaya (Sarpkaya, 2004), Williamson and Govardhan (Williamson and Govardhan, 2004) and Bearman (Bearman, 2011). Generally, the main focus of these studies is to determine the maximum displacement response of the structures. Because the possible failure of a structure occurs due to response of the structure subjected to VIV.

For simplicity, these structures are often modelled as linear spring damping system of freely vibrating cylinder with one or more degree of freedom. VIV is associated most with the term “lock-in” phenomenon that means the vortex shedding frequency is dominating the structure near the system’s natural frequency. Extensive researches have been done to understand the physics and the dependent parameters of VIV.

Feng (Feng, 1968), conducted experiments with relatively high mass-damping,  $m^*\zeta$ , and found two response characteristics over a range of reduced velocity ( $U_r$ ) and concluded that there are two response branches namely “initial” and “lower” branch.

To provide insight into the possible maximum amplitude and further investigate effect of different mass-damping,  $m^*\zeta$ , of a cylinder, Khalak and Williamson (Khalak and Williamson 1996, 1997, 1999), conducted series of experiments with different  $m^*\zeta$ . They figured out that there are three response characteristics, namely “initial”, “upper” and “lower” branches, exist for VIV of a cylinder with very low mass-damping,  $m^*\zeta$ , (Khalak and Williamson, 1996). In their experiments, they found that maximum dimensionless amplitude,  $A^*$ , is close to 1 during lock-in for very low mass-damping ( $m^*\zeta$ ). However, they also found that there are two types of responses. For high  $m^*\zeta$ , systems, the upper branch is absent and only initial and lower branches exist (Khalak and Williamson, 1999). They found that, the peak amplitude is mainly dependent on the  $m^*\zeta$ , where the regime of lock-in for given value of  $m^*\zeta$ , is dependent mainly on the mass ratio,  $m^*$ , only.

The frequency of the shedding and the displacement is nearly the same during lock-in and the frequency ratio,  $f^*$ , which is the ratio of displacement of cylinder to the natural frequency of the system's natural frequency, was found 1.4 for mass ratio,  $m^* = 2.4$  (Khalak and Williamson, 1997). But for  $m^*\zeta$ , systems it was found closer to unity (Khalak and Williamson, 1999).

The transition from between branches was found that it is related to vortex shedding patterns and phase change (Williamson and Roshko, 1988). The transition of initial to upper branch was found to be hysteric and upper to lower branch transition corresponds to a  $0^\circ$  to  $180^\circ$  phase change (Khalak and Williamson, 1999). Also, they found initial branch corresponds to 2S (two single vortices per cycle) mode while the lower branch is corresponding to 2P (two pair of vortices per cycle) mode.

However, Govardhan and Williamson (Govardhan and Williamson, 2000) discussed that total fluid force on the oscillating system consist of two forces, namely; lift and vortex forces. The initial to upper branch transition is consisting of  $180^\circ$  phase

change in vortex force and upper to lower branch transition corresponds to a  $0^\circ$  to  $180^\circ$  phase change in lift force. They also found that upper branch is 2P mode with one of vortices in the pair which is smaller than the other.

Klamo et al. (Klamo et al., 2005) and Govardhan and Williamson (Govardhan and Williamson, 2006) demonstrated the strong influence of the Reynolds number. Until their study, it was believed that Reynolds number has a minor effect on VIV.

To investigate the effect of damping, Klamo et al. (Klamo et al., 2006), showed the transition between three branch responses to two branch responses with higher damping values. They concluded that three branch response is observed with low  $m^*\zeta$  and at high Re number and as the damping increases, two branch response occurs.

Over the years with development on the numerical methods, VIV was also investigated by numerical methods. Numerical methods are very efficient ways to investigate the VIV phenomenon by means of cost and time.

Earlier studies focused on relatively low Reynolds numbers (Blackburn and Karniadakis, 1993; Newman and Karniadakis, 1997; Saltara et al., 1998 and Evangelinos, 1999) contrary of the experiments with higher Reynolds number.

With higher Reynolds numbers, two notable numerical studies were done by Guilmineau and Queutey (Guilmineau and Queutey, 2004) and Pan et al. (Pan et al., 2007). They investigated 2D simulation VIV of a cylinder with same parameters as Khalak and Williamson (Khalak and Williamson, 1996). Although their studies were overall in good agreement with the experimental results, the maximum amplitude responses were not well captured.

More recent, it is possible to reach studies about 2D simulation of VIV done by various researchers (Li et al. 2014; Kang et al., 2017 and Khan et al., 2018,).

Li et al. (Li et al., 2014) compared different turbulence models and concluded that SST k-w turbulence model was in good agreement with the experimental data of Khalak and Williamson (Khalak and Williamson, 1996).

Kang et al. (Kang et al., 2017) used a modified SST model to capture maximum amplitude of VIV of 2D cylinder with 2DOF. They showed that their improved SST

model were in good agreement with the experimental study by Jauvtis and Williamson (Jauvtis and Williamson, 2004).

Khan et al. (Khan et al., 2018) investigated different turbulence model of VIV both for 2D and 3D cylinder. They concluded, k-w SST model is overall in well agreement with both experimental data (Hover et al., 1997) and numerical study (Nguyen et al., 2016).

## **1.2 Objective of the Thesis**

Objective of this thesis is to simulate 1DOF VIV in transverse direction using URANS method of a 2D cylindrical structural by changing its structural damping ratio and to compare the results with experimental study by Soti et al. (Soti et al., 2018). The damping ratio one of the most important parameter that affects the vibration amplitude of the structural system. To better understand these effects, damping ratio is chosen to investigate in this study.

## **1.3 Hypothesis**

Soti et al. (Soti et al., 2018) shows that with increased damping coefficient, the amplitude and the lock-in region interval of the VIV of a cylindrical structure is changed. Also, there is a delay occurred in the transition from initial branch to upper branch with the increased damping.

The present study aims to investigate numerically, whether the same effects can be observed or not.

## Theoretical Background of Vortex-Induced Vibration

---

### 2.1 Regime of Flow

One of the most important parameters related to the flow around a cylinder is Reynolds number,  $Re$ , which is a dimensionless parameter that represents a measure of the inertia forces over viscous forces.  $Re$  number can be expressed as;

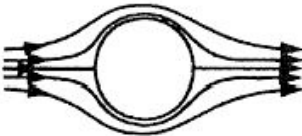
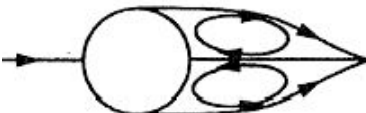
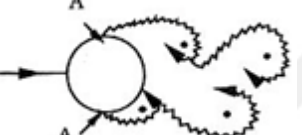
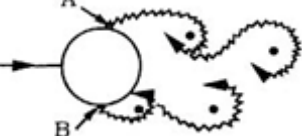
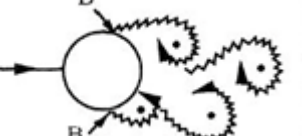
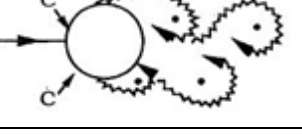
$$Re = \frac{U_{\infty} D}{\nu} \quad (2.1)$$

As the  $Re$  number changes significantly, different flow regimes develop. When  $Re$  is very low ( $Re < 5$ ) no flow separation occurs. As  $Re$  number value increases flow becomes unstable and separation occurs. These events lead to periodic vortices formation. As a result, wake region occurs as a vortex street. Regime of flow for a cylindrical structure is shown in Table 2.1.

### 2.2 Vortex Shedding

According to Sumer and Fredsøe (Sumer and Fredsøe, 1997), when  $Re$  exceeds 40, the boundary layer over the cylinder will start to separate due to the adverse pressure gradient change at the rear side of the cylinder. This pressure gradient change causes the shear layer in the wake region to roll up into a vortex structure. Consequently, this event leads to periodic development of vortices. These vortices produce a wake pattern that is called as Kármán vortex street named after von Kármán for fixed cylinder.

**Table 2.1** Regimes of flow around a cylindrical structure in steady flow (Sumer & Fredsøe, 1997)

	No separation Creeping flow	$Re < 5$
	A fixed pair of symmetric vortices	$5 < Re < 40$
	Laminar vortex street	$40 < Re < 200$
	Transition to turbulence in the wake	$200 < Re < 300$
	Wake completely turbulent A: Laminar boundary layer separation	$300 < Re < 3 \times 10^5$ Subcritical
	A: Laminar boundary layer separation B: Turbulent boundary layer separation: but boundary layer laminar	$3 \times 10^5 < Re < 3.5 \times 10^5$ Critical (Lower transition)
	B: Turbulent boundary layer separation: the boundary layer partly laminar, partly turbulent	$3.5 \times 10^5 < Re < 1.5 \times 10^6$ Supercritical
	C: Boundary layer completely turbulent at one side	$1.5 \times 10^6 < Re < 4 \times 10^6$ Upper transition
	C: Boundary layer completely turbulent at two sides	$4 \times 10^6 < Re$ Transcritical

This vortex shedding happens periodically. Hence, it has a certain frequency, which is called the vortex shedding frequency,  $f_v$ :

$$f_v = \frac{1}{T_v} \quad (2.2)$$

This frequency depends on the Reynolds number.

Vortex shedding frequency is normalized by the definition of Strouhal number,  $St$ .

$$St = \frac{f_v D}{U} \quad (2.3)$$

It is used as a measure of predominant vortex shedding frequency.

### 2.3 Lift and Drag Forces

As vortex shedding changes periodically, the pressure on the surface of the cylinder also has a periodic change, hence generating a periodic change in the forces on the cylinder surface. The force of the pressure distribution can be divided into two components which are transverse lift force ( $F_L$ ) and in-line drag force ( $F_D$ ).

The lift force occurs when the vortex shedding starts. It oscillates as same as the vortex shedding frequency. Concurrently, the drag force fluctuates like lift force. Due to this fluctuation, the surface of cylinder has a force difference acting on it because of pressure difference between upstream and downstream faces of the cylinder. This is the reason why drag force oscillates around the mean drag.

To express lift force and drag force as a dimensionless parameter; coefficient of lift,  $C_L$ , and coefficient of drag,  $C_D$ , can be formulated as below:

$$C_L = \frac{F_L}{\frac{1}{2}\rho L D U^2} \quad (2.4)$$

$$C_D = \frac{F_D}{\frac{1}{2}\rho L D U^2} \quad (2.5)$$

### 2.4 Vortex-Induced Vibration

When a flexibly mounted bluff body exposes a crossflow, it starts to oscillate due to fluctuating vortex shedding from rear side of the cylinder as these vortices exert a periodic force on the cylinder surface. This phenomenon is called Vortex-Induced Vibration.

The amplitude of VIV for a cylinder depends on many parameters namely, drag, lift, stiffness, damping coefficient and mass ratio which are explained in the following chapters. There are various investigation methods for VIV that cover single or multi degree of freedom motion by both numerical and experimental procedures. In this study, cylindrical structure is free to move only in transverse direction.

Structures which have circular cross-section are used by many researchers to study VIV for engineering applications. These systems can be represented by a linear mass-spring system. In Figure 2.1, VIV of a cylindrical cross section is represented as a 1DOF model to move in the transverse ( $y$ ) direction as a mass-spring-damper system. Where  $D$  is the diameter of the cylinder,  $k_s$  is stiffness coefficient and  $c$  is damping coefficient.

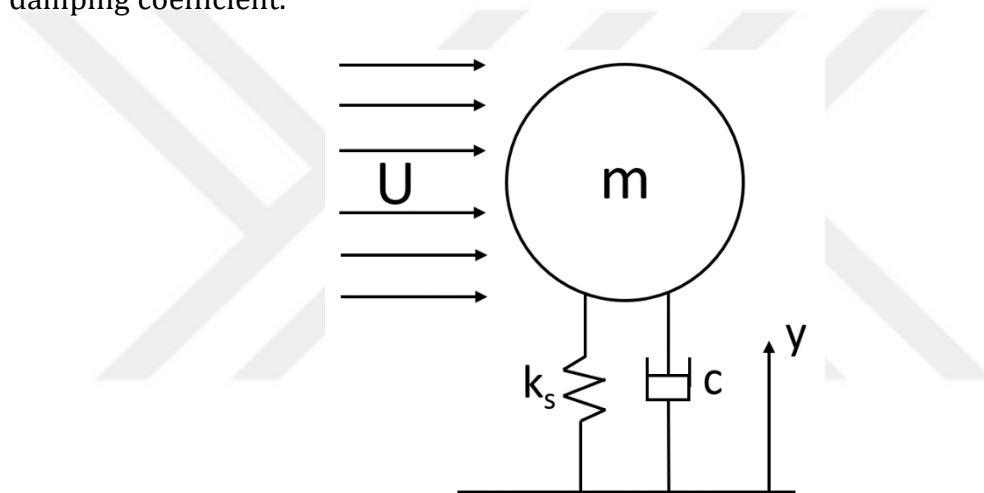


**Figure 2.1** Schematics of physical model

## 2.5 Vortex Patterns

Vortex patterns are one of the most important aspects of VIV. It is an indication of branch change of the system's response. When Re number increases beyond 40, periodic vortices begin to shed from the downstream part of the cylinder comprise a region known as the von Kármán vortex street. However, if cylinder oscillates in the transverse direction the patterns are different from the classical von Kármán street. These various patterns were investigated by Williamson and Roshko (Williamson and Roshko, 1988) as seen in Figure 2.2.

The labeling S and P indicates, single and pair of vortices per cycle, respectively. The types of the patterns depend on two parameters; dimensionless amplitude ( $A^*=A/D$ ) and wave length ratio ( $\lambda^*=\lambda/D$ ).

The studies show that initial branch is associated with 2S mode and the upper and lower branch are associated with 2P mode.

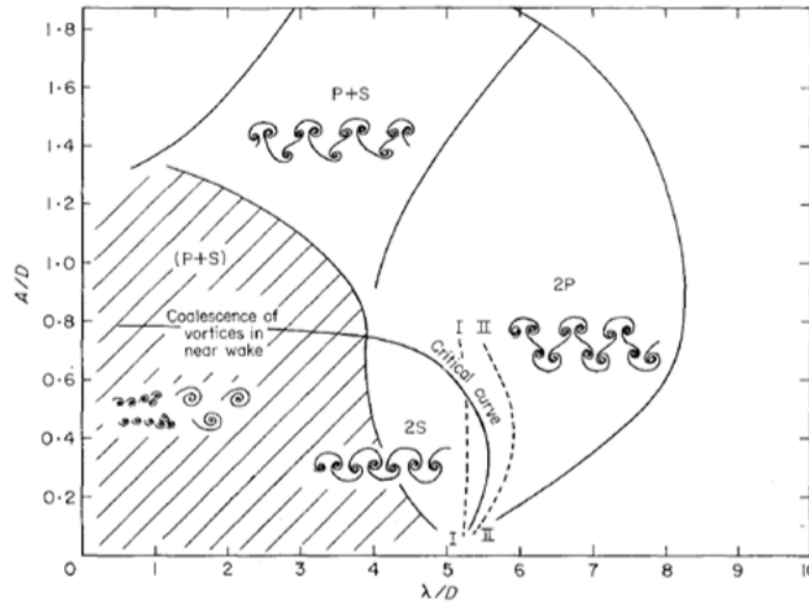


**Figure 2.2** Map of vortex pattern as a function of dimensionless amplitude and wave length ratio (Williamson and Roshko, 1988)

## 2.6 Dynamics of 1DOF System

In this study, the structure is modeled as an elastically mounted cylindrical structure with free to move in the transverse direction only. System's equation of motion is represented by an idealized linear equation of a mass-spring-damper system.

Equation of motion can be expressed in y direction as:

$$m\ddot{y} + c\dot{y} + k_s y = F_y \quad (2.6)$$

where, m is the mass of the cylinder, y is the position of the cylinder measured from the initial position,  $k_s$  is the stiffness coefficient, c is the damping coefficient and  $F_y$  is fluctuating transverse (y direction) force exerted by fluid forces.

Assuming cylinder has a sinusoidal motion due to fluctuating fluid forces, the solution of the system, equation of motion in y direction is;

$$y(t) = A \sin(\omega_n t + \phi) \quad (2.7)$$

$$\omega_n = 2\pi f_n \quad (2.8)$$

Where A is maximum amplitude determined from initial condition,  $\omega_n$  is system's angular natural frequency in water,  $f_n$  is system's natural frequency in water, and  $\phi$  is the phase angle between fluid forces and the displacement of the cylinder.

The fluid forces exerted on the cylinder can be expressed as;

$$F_y(t) = F_0 \sin \omega_d t \quad (2.9)$$

Where  $F_0$  maximum force,  $\omega_d=2\pi f$  is the body oscillation angular frequency. From equations 2.6 to 2.9 the dimensionless amplitude,  $A^*$ , and frequency ratio,  $f^*$ , equations can be expressed as (Govardhan and Williamson, 2000);

$$A^* = \frac{1}{4\pi^3} \frac{C_L \sin \phi}{(m^* + C_A)\zeta} \left(\frac{U_r}{f^*}\right) f^* \quad (2.10)$$

$$f^* = \sqrt{\frac{m^* + C_A}{m^* + C_{EA}}} \quad (2.11)$$

Where;

$$A^* = \frac{A}{D} \quad (2.12)$$

is the dimensionless amplitude,

$$m^* = \frac{m}{\frac{1}{4}\pi\rho D^2 L} \quad (2.13)$$

is the mass ratio which is the ratio of system's mass (cylinder mass) over the displaced fluid mass ( $m_d=\pi\rho D^2 L/4$ ),

$$f^* = \frac{f}{f_n} \quad (2.14)$$

is the dimensionless frequency;  $f=\omega/2\pi$  body oscillation frequency and

$$f_n = \frac{1}{2\pi} \sqrt{\frac{k_s}{m+m_A}} \quad (2.15)$$

is natural frequency of the system in water where  $m_A= C_A m_d$  ( $C_A=1$  potential added mass coefficient for cylinder) is added mass,

$$Ur = \frac{U}{f_n D} \quad (2.16)$$

is the reduced velocity,

$$\zeta = \frac{c}{c_{crit}} = \frac{c}{2\sqrt{k_s(m+m_A)}} \quad (2.17)$$

is the structural damping ratio, where  $c$  is damping coefficient,

$$C_{EA} = \frac{1}{2\pi^3} \frac{C_L \sin \phi}{A^*} \left( \frac{U_r}{f^*} \right) \quad (2.18)$$

is effective added mass coefficient,

$$\phi = \tan^{-1} \left( \frac{2\zeta f^*}{1-(f^*)^2} \right) \quad (2.19)$$

is the phase angle between fluid forces and the cylinder displacement.

Table 2.2 shows the main dimensionless parameters used in this study as a summary.

## 2.7 Effect of Mass Ratio

The mass ratio of previous studies determined based on the fluid medium, whether water or air. Sumer and Fredsøe (Sumer and Fredsøe, 1997) conducted experiments in both water and air medium and concluded that in the air medium the frequency ratio,  $f$ , is equal to unity during lock-in. However, in water medium the ratio is higher than unity. Figure 2.3 shows the frequency response in air and water.

Bearman (Bearman, 2009), conducted experiments on smaller mass ratios and showed that smaller mass ratio causes higher amplitude response of the system. Also, Khalak and Williamson (Khalak and Williamson, 1999) shows that, with varying mass ratio, there are two types of response; at low mass ratio there are three branches exist namely, initial, upper and lower branches. For higher mass ratio, only two branches exist; initial and lower branches. Figure 2.4 shows these responses with comparison of Feng (Feng, 1968) data.

**Table 2.2** Dimensionless Parameters

Reynolds number ( $Re$ )	$Re = \frac{U\mu D}{\rho}$
Strouhal number ( $St$ )	$St = \frac{f_v D}{U}$
Lift Coefficient ( $C_L$ )	$C_L = \frac{F_L}{\frac{1}{2}\rho LDU^2}$
Drag Coefficient ( $C_D$ )	$C_D = \frac{F_D}{\frac{1}{2}\rho LDU^2}$
Dimensionless Amplitude ( $A^*$ )	$A^* = \frac{A}{D}$
Mass ratio ( $m^*$ )	$m^* = \frac{m}{\frac{1}{4}\pi\rho D^2 L}$
Frequency ratio ( $f^{**}$ )	$f^* = \frac{f}{f_n}$
Reduced velocity ( $U_r$ )	$Ur = \frac{U}{f_n D}$
Natural frequency ( $f_n$ )	$f_n = \frac{1}{2\pi} \sqrt{\frac{k_s}{m + m_A}}$
Structural damping ratio ( $\zeta$ )	$\zeta = \frac{c}{2\sqrt{k_s(m + m_A)}}$
Phase angle ( $\phi$ )	$\phi = \tan^{-1} \left( \frac{2\zeta f^*}{1 - (f^*)^2} \right)$

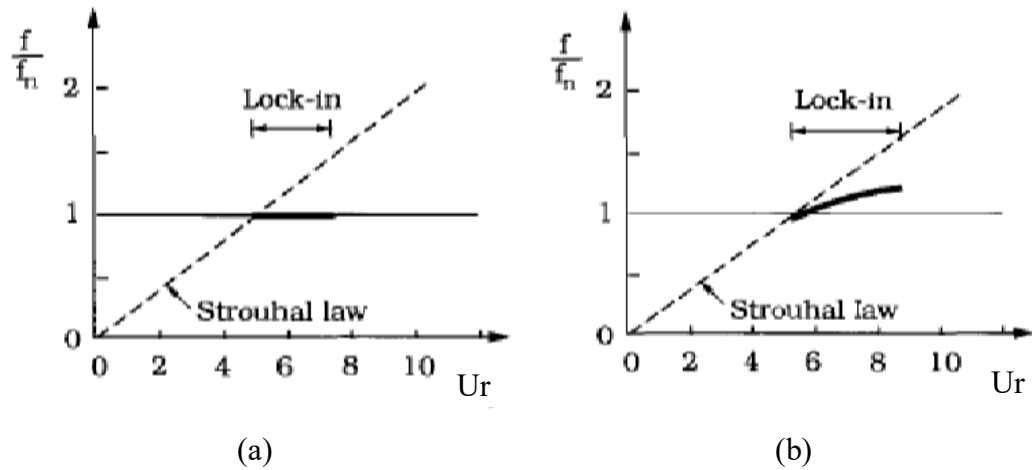


**Figure 2.3** Frequency ratio,  $f^*=f/f_n$ , in air (a) and water (b) as a function of  $Ur$  (Sumer and Fredsøe, 1997)

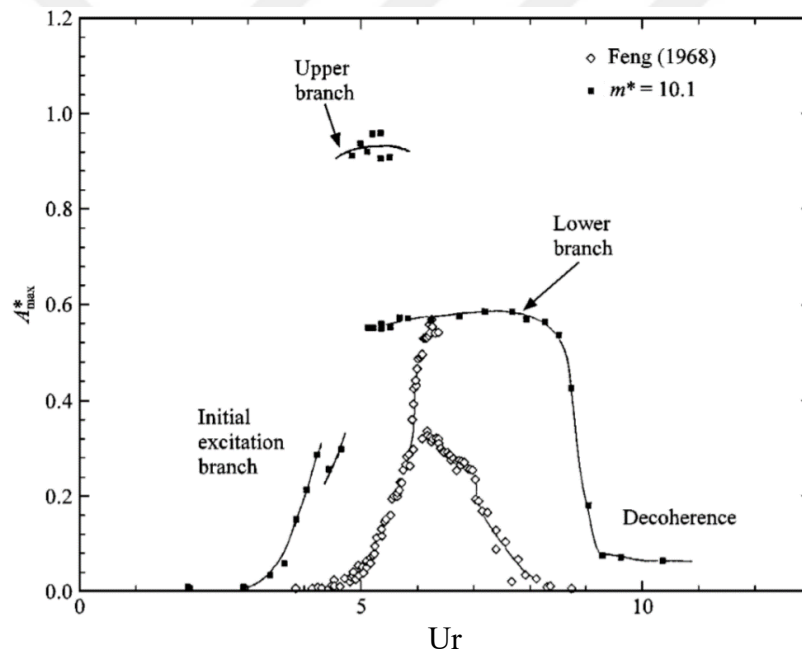


**Figure 2.4** Dimensionless amplitude,  $A^*$ , as a function of  $Ur$  of different mass ratios ( $m^*=10.1$  Kahlak and Williamson, 1999,  $m^*=248$  Feng, 1968)

### 2.8 Effect of Aspect Ratio

The aspect ratio of a system is defined by  $A_s = L/D$  where  $L$  is the length of the cylinder and  $D$  is the diameter of the cylinder. In current study  $L$  is taken as 1, due to 2D simulation domain.

Rahman and Thiagarajan (Rahman and Thiagarajan, 2015) conducted series of experiments to understand effect of the aspect ratio. They showed that the amplitude of response of the structure decreases with lower aspect ratio and the range of lock-in getting narrower with decreased aspect ratio. Figure 2.5 shows the effect of different aspect ratio for system's response. Also, it is important to mention that experiment with  $L/D=13$  was done with different damping setting, that's why it is different from the general trend.

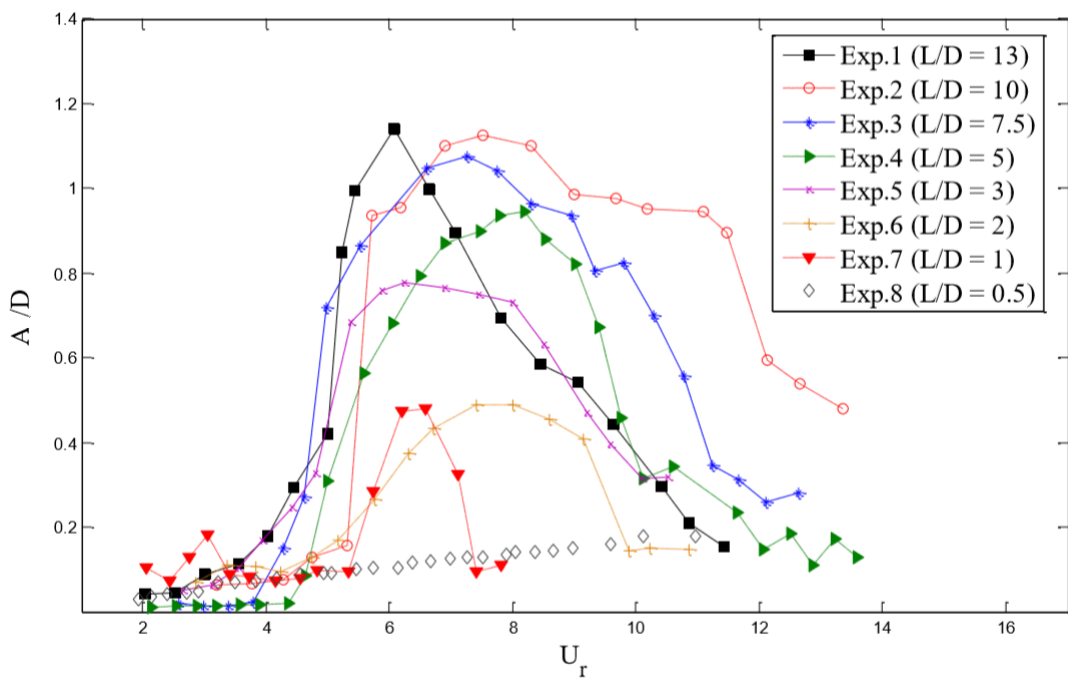


**Figure 2.5** Dimensionless amplitude,  $A^*=A/D$ , as a function of  $U_r$  with different aspect ratios (Rahman and Thiagarajan, 2015)

### 3.1 Introduction

With the recent development of computer technologies, computational fluid dynamics (CFD) codes are being accepted as an industrial standard in many engineering applications in design phase. Today, many industries use CFD codes as a design tool.

Unlike more expensive and difficult methods (Model testing facilities or experimental laboratories), CFD simulations provide vast variety of test scenarios and design possibilities with no model scale limitation, cost and time efficiency.

This chapter covers the fundamentals of the fluid dynamics which are essential to understand the CFD methods.

### 3.2 Fundamentals of Fluid Dynamics

#### 3.2.1 Conservation of Mass

In fluid dynamics, conservation of mass principle states that, the rate of the mass that enters the system is same as the mass leave from the system in a closed system. The conversation of mass can be expressed as;

$$\frac{\partial \rho}{\partial t} + \nabla \cdot (\rho \vec{u}) = 0 \quad (3.1)$$

When the fluid is assumed incompressible also means that the density does not change with respect to time,  $\rho = \text{constant}$ , Equation 3.1 can be simplified as;

$$\nabla \cdot \vec{u} = 0 \quad (3.2)$$

In this study, fluid is assumed as incompressible.

### 3.2.2 Conservation of Momentum

In fluid dynamics, from Newton's second law, conservation of momentum principle indicates that total momentum of a closed system does not change if there is no external force. Also, the rate of change of momentum is equal total sum of the forces acting on fluid particles.

The conservation of momentum can be express in x, y and z directions respectively as;

$$\frac{\partial(\rho u)}{\partial t} + \nabla \cdot (\rho u \vec{u}) = \nabla \cdot (\mu \nabla u) - \frac{\partial p}{\partial x} + \rho g_x \quad (3.3)$$

$$\frac{\partial(\rho v)}{\partial t} + \nabla \cdot (\rho v \vec{u}) = \nabla \cdot (\mu \nabla v) - \frac{\partial p}{\partial y} + \rho g_y \quad (3.4)$$

$$\frac{\partial(\rho w)}{\partial t} + \nabla \cdot (\rho w \vec{u}) = \nabla \cdot (\mu \nabla w) - \frac{\partial p}{\partial z} + \rho g_z \quad (3.5)$$

The term  $\rho g$  represents the forces acting on fluid particle. These equations are also called the Navier-Stokes equations.

### 3.3 CFD Methodology

CFD simulations consist of three main stages namely; pre-processing, solving and post-processing.

At the first stage, which is pre-processing, the all aspects of the problem are defined, like grid generation in the solution domain (meshing), specifying the boundary conditions, fluid properties, physical conditions, solver types and settings etc.

In the second stage, which is solving, the problem is solved by various numerical methods. There are three different numerical methods for solving simulations which are finite element method, finite difference method and finite volume method. The differences of these numerical methods are due to approximation of the variables and the discretization process. In commercial CFD codes, the most common numerical method implemented is the finite volume method (FVM). FVM discretizes the solution domain into the continuous control volumes (mesh) and the fundamental equations are solved for every control volume by integration and interpolation.

At the last stage, which is post-processing, the results are evaluated with various tools, like contour and vector plots, animations, particle tracking etc.

In this study a commercial CFD software ANSYS Fluent is used for all simulations. It is one of the most common and powerful software for CFD simulations.

### **3.4 Turbulence Modelling**

Turbulence is the unsteady random fluid flow that occurs at higher Reynolds numbers. Although turbulence is expressed by the Navier-Stokes equations, it needs to be solved with approximations and averaging procedures due to its high non-linearities. With continuous development of the computer technology, the availability of powerful computers gives researchers many opportunities to study various turbulence problems in fluid dynamics. To simulate turbulence, there are various turbulence models for different problems (Kajishima and Taira, 2017). These models are;

- One equation RANS (Reynolds-Averaged Navier-Stokes) turbulence model; The Spalart-Allmaras Model
- Two equations RANS (Reynolds-Averaged Navier-Stokes) turbulence models; k- $\epsilon$ , RNG k- $\epsilon$ , Realizable k- $\epsilon$ , k- $\omega$ , SST k- $\omega$  etc.
- Large Eddy Simulations (LES)
- Reynolds Stress Model (RSM)
- Detached Eddy Simulation (DES)

One of the most efficient and widely used turbulence modeling method is the RANS method for moderate Reynolds number. Also, previous studies show that for VIV, one of the RANS model, SST k- $\omega$  turbulence model is in good agreement with the experimental data for 2D simulations (Guilmineau and Queutey, 2004 and Pan et al., 2007). In this study, SST k- $\omega$  turbulence model is used for all simulations.

#### **3.4.1 SST k- $\omega$ Turbulence Model**

As mentioned before, RANS models offer the most efficient turbulence modeling approach, since it is computationally inexpensive, and level of accuracy is good enough for most engineering applications. In general, RANS models simplify the problem by adding two additional transport equations and introduce a turbulent viscosity to compute the Reynolds Stresses. Reynolds stresses are additional unknowns that arise from the time averaging of the Navier-Stokes equations. They

are the product of the instantaneous turbulent velocity fluctuations in fluid momentum. They must be modeled in order to close the system of governing equations. RANS models close the system via calculating turbulent viscosity with transport equations depending on the RANS model.

k- $\omega$  is one of the RANS models based on Wilcox (Wilcox, 1988) model. It is a two-equation model that transport equations solved by turbulent kinetic energy (k) and the specific dissipation rate ( $\omega$ ). k- $\omega$  models give more robust solutions for boundary layer flows and boundary separation problems like VIV.

The turbulence kinetic energy, k, and its dissipation rate,  $\omega$ , are derived from the following transport equations:

$$\frac{\partial}{\partial t}(\rho k) + \frac{\partial}{\partial x_i}(\rho k u_i) = \frac{\partial}{\partial x_j}(\Gamma_k \frac{\partial k}{\partial x_j}) + G_k - Y_k + S_k \quad (3.6)$$

and

$$\frac{\partial}{\partial t}(\rho \omega) + \frac{\partial}{\partial x_i}(\rho \omega u_i) = \frac{\partial}{\partial x_j}(\Gamma_\omega \frac{\partial \omega}{\partial x_j}) + G_\omega - Y_\omega + S_\omega \quad (3.7)$$

All of the above terms are calculated as described below.  $S_k$  and  $S_\omega$  are user-defined source terms (ANSYS Fluent Theory Guide, 2019).

The effective diffusivities for the k-  $\omega$  model are given by

$$\Gamma_k = \mu + \frac{\mu_t}{\sigma_k} \quad (3.8)$$

$$\Gamma_\omega = \mu + \frac{\mu_t}{\sigma_\omega} \quad (3.9)$$

where  $\sigma_k$  and  $\sigma_\omega$  are the turbulent Prandtl numbers for k and  $\omega$ , respectively and  $\mu_t$  is turbulent viscosity. One of the biggest negative aspect of the standard k- $\omega$  is the dependence to the free-stream values k and  $\omega$  outside the shear layer (ANSYS Fluent Theory Guide, 2019).

Menter (Menter, 1994) developed k- $\omega$  shear stress transport (SST) model to avoid this free-stream sensitivity. It combines the robustness of k- $\omega$  near wall and the k- $\epsilon$  model outside the near wall (ANSYS Fluent Theory Guide, 2019).

With these features, the SST k- $\omega$  model is more suited for adverse pressure gradient and separation problems than the standard one.

### 3.4.2 Near Wall Boundary Layer

Aside from the proper turbulence model, the accuracy also depends on the boundary layer. The mesh resolution near cylinder has to be fine enough near its boundary layer to model the problem accurately. A dimensionless parameter,  $y^+$ , for the estimation of the first layer height can be expressed as;

$$y^+ = \frac{y_f U_\tau}{\nu} \quad (3.10)$$

Figure 3.1 shows the type of flows as a function of dimensionless velocity,  $u^+=U/U_\tau$  and  $y^+$ .

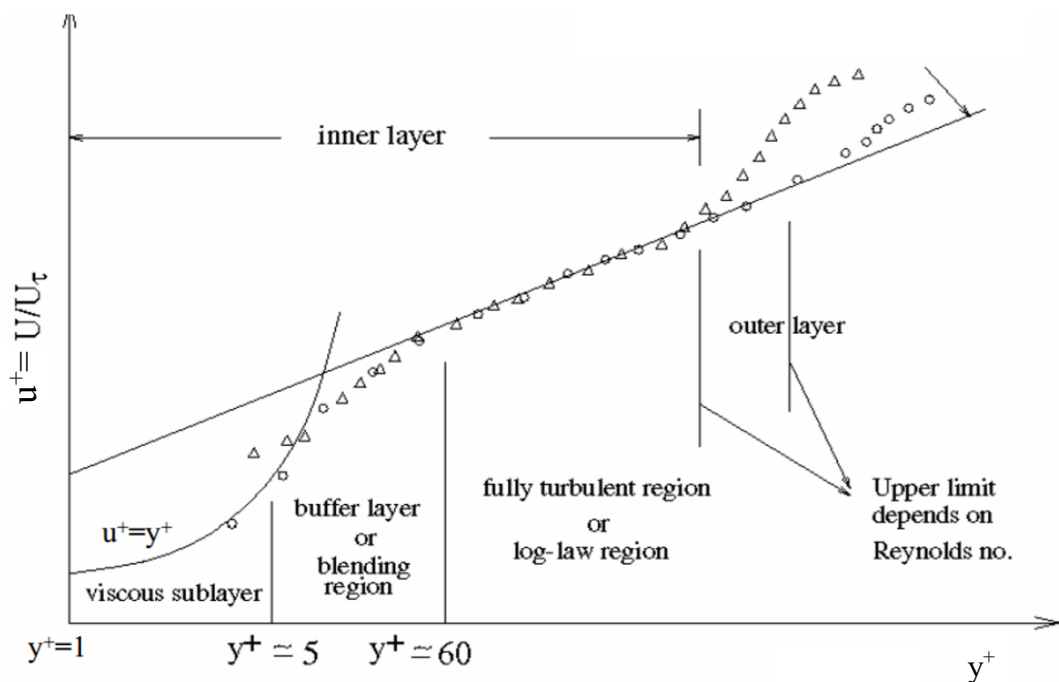


**Figure 3.1** Types of flows and suggested  $y^+$  values. (Anderson, 1995)

To get accurate results near the wall, a resolution of  $5 < y^+$  is suggested since SST  $k-\omega$  model is used and the viscous sublayer to be captured (ANSYS Fluent Theory Guide, 2019).

### 3.5 Pressure - Velocity Coupling

There are four segregated types of pressure-based algorithms in ANSYS Fluent for iterative solutions, namely; SIMPLE, SIMPLEC, PISO and Non-Iterative Time Advancement option (NITA); Fractional Step Method (FSM). In this study PISO pressure - velocity coupling algorithm is used.

The Pressure-Implicit with Splitting of Operators (PISO) pressure-velocity coupling scheme, which is a part of the SIMPLE family of algorithms, is based on the higher degree of the approximate relation between the corrections for pressure and velocity. One of the limitations of the SIMPLE and SIMPLEC algorithms is that new velocities and corresponding fluxes which do not satisfy the momentum balance after the pressure correction equation is solved. As a result, the calculation must be repeated until the balance is satisfied. To improve the efficiency of this calculation, the PISO algorithm performs two additional corrections. These correction steps are applied in order to get more accurate results of SIMPLE procedure (ANSYS Fluent Theory Guide, 2019).

PISO is recommended for transient calculations (ANSYS Fluent Theory Guide, 2019). In this study all simulations are performed with the PISO algorithm. Also, to speed up the convergence and the capture to unsteadiness, pressure under-relaxation factor increased to 0.7 from default value of 0.3 as suggested. Figure 3.2 shows the solution method for segregated pressure-based solver.

### **3.6 Discretization Schemes**

In CFD simulations, ANSYS Fluent uses a control-volume-based technique to convert a general scalar transport equation to an algebraic equation that can be solved numerically. This control volume technique consists of integrating the transport equation about each control volume, yielding a discrete equation that expresses the conservation law on a control-volume basis (ANSYS Fluent Theory Guide, 2019).

#### **3.6.1 Spatial Discretization**

FVM method divides the solution domain into small domains by applied mesh. Solver stores discrete values at the cell centers. However, face values at each cell that are required for the convection terms must be interpolated from the cell center values. This is accomplished using an “upwind scheme”.

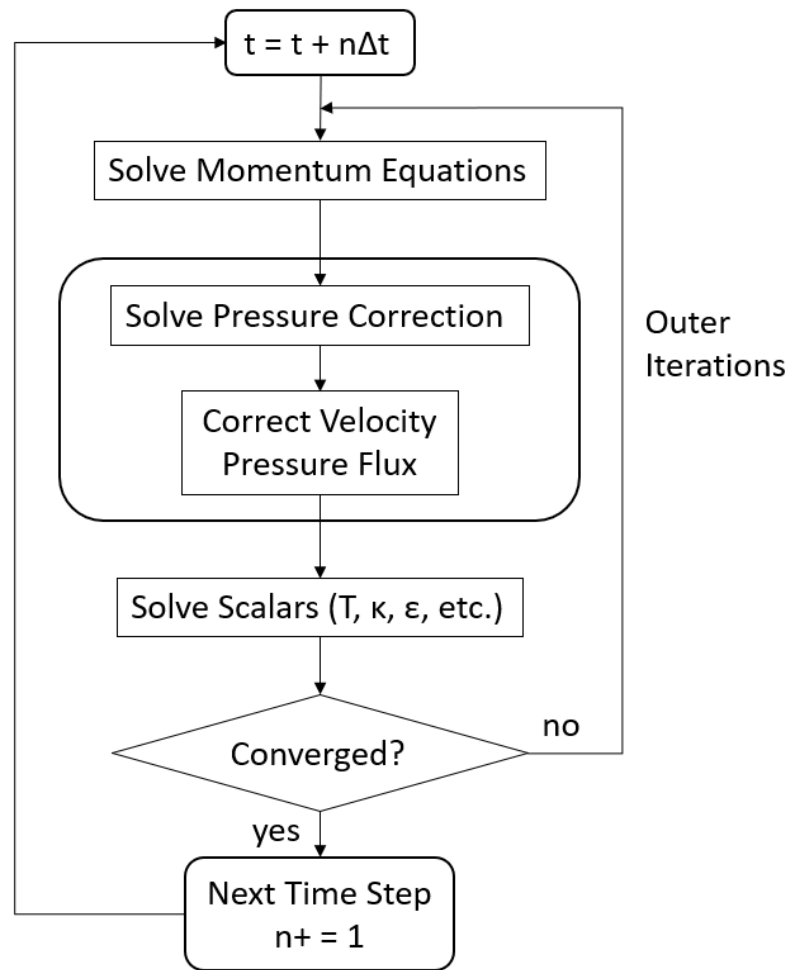


**Figure 3.2** Overview of iterative segregated pressure-based solver (ANSYS Fluent Theory Guide, 2019)

Upwinding means that the face value is derived from quantities in the cell upstream, or “upwind,” relative to the direction of the normal velocity. In ANSYS Fluent the upwind schemes are; first-order upwind, second-order upwind, power law, and QUICK (ANSYS Fluent Theory Guide, 2019).

In this study all the spatial discretization schemes are chosen second-order upwind to maintain accuracy and computational efficiency.

### 3.6.2 Temporal Discretization

All of the simulations in this study are time dependent transient simulations. Thus, all simulations are also required to be discretized in time domain. Temporal discretization is also chosen as second-order upwind scheme.

In addition to temporal discretization, to maintain the stability and the accuracy of the solution a proper time step must be chosen. To choose a proper time step a dimensionless parameter Courant number needs to be kept around 1. Courant number,  $C$ , can be express as in the lateral ( $x$ ) direction as;

$$C = \frac{U\Delta t}{\Delta x} \quad (3.11)$$

Where,  $U$  is free- stream velocity,  $\Delta t$  is time step and  $\Delta x$  is mesh size in  $x$  direction. For all the simulations in this study, a time step is chosen as that  $C$  is kept around 1.

### 3.7 Dynamic Mesh Methods

Since the purpose of this work is to study VIV of a cylinder, a dynamic mesh solver needs to be implemented to the solving stage in order to capture the displacement amplitude response of the cylinder. Therefore, ANSYS Fluent's 6DOF solver is implemented in the simulations by a user-defined function (UDF). UDF is used to represent the physical properties of the cylindrical mass-spring-damper system and the net force acting on the cylinder.

There are three dynamic mesh update methods in ANSYS Fluent which are remeshing, layering and smoothing. Since in this work structured mesh is used, the smoothing with diffusion method is chosen as suggested, since it provides more uniform deforming mesh.

When smoothing is used to adjust the mesh of a zone with a moving and/or deforming boundary, the interior nodes of the mesh move, but the number of nodes and their connectivity do not change. In this way, the interior nodes "absorb" the movement of the boundary (ANSYS Fluent Theory Guide, 2019).

As for the diffusion type smoothing, there are two formulations for diffusion coefficient in ANSYS Fluent. To maintain the boundary layer stability, diffusion formulation is chosen as boundary-distance and the diffusion parameter is set to 1. The diffusion parameter value (1) provides more uniform deformation throughout the mesh. As diffusion parameter is set to 1, the mesh around the cylinder deforms less. Consequently, it is ensured that dynamic mesh does not influence the expected  $y^+$  value near cylinder surface.

#### 4.1 Solution Domain and Mesh Generation

One of the most important aspects of a CFD simulation is the solution domain and the grid generation. For this study, the solution domain size has to be adequate for the fully developed flow and the existence of the boundaries must not affect or change the results. Cylinder diameter is taken as  $D=1\text{m}$ . The computational domain extends  $15D$  from cylinder for the inlet of the domain,  $25D$  behind the cylinder and  $10D$  for both upper and lower boundaries where  $D$  is diameter of the cylinder. Figure 4.1 shows the solution domain dimensions. Outlet side of solution domain size is chosen to ensure fully vortex street development. As for the inlet and the upper and lower wall, the domain size is chosen as boundaries that do not affect the flow.

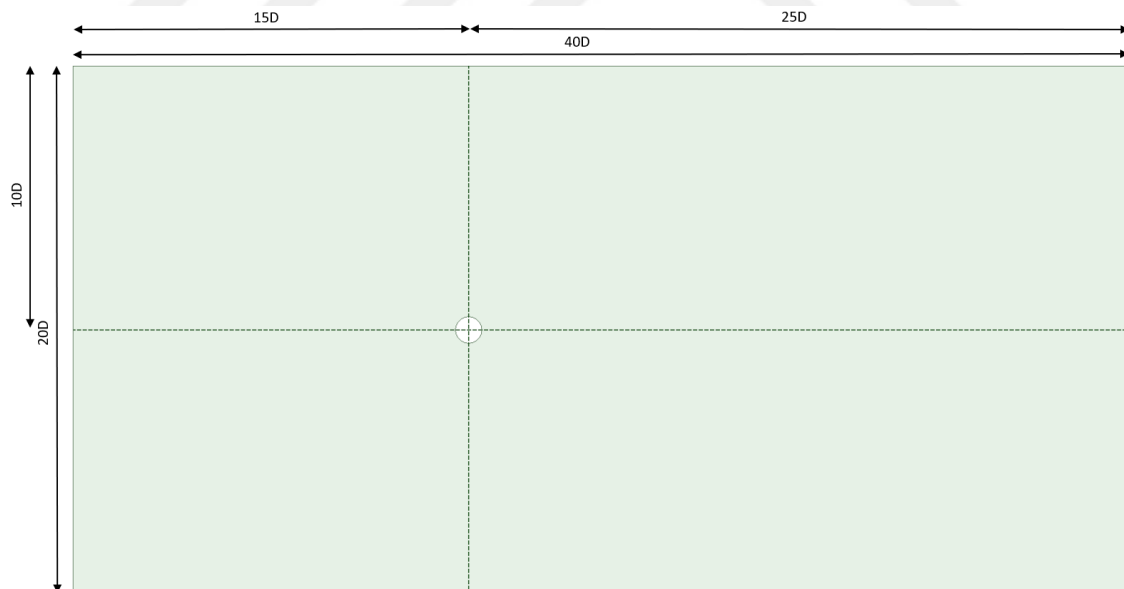


**Figure 4.1** Solution domain

Solution domain is discretized with structured hexagonal elements for better accuracy. Figure 4.2 shows the mesh structure of the domain. Also, as shown in

Figure 4.3 cylinder boundary layer is denser with inflation method to maintain  $y^+$  around 1.

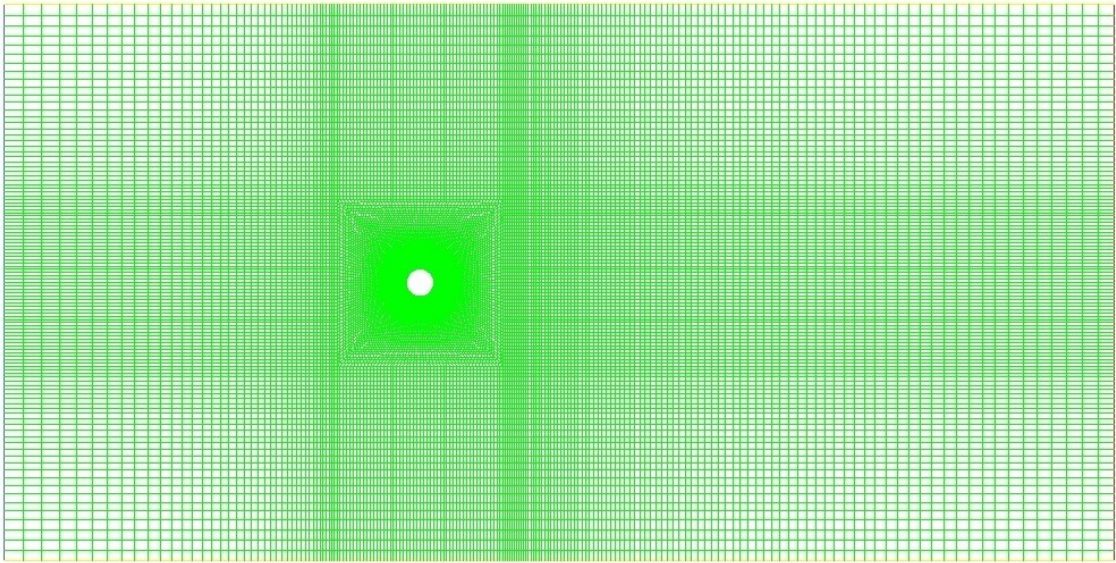


**Figure 4.2** Mesh structure applied to the computational domain

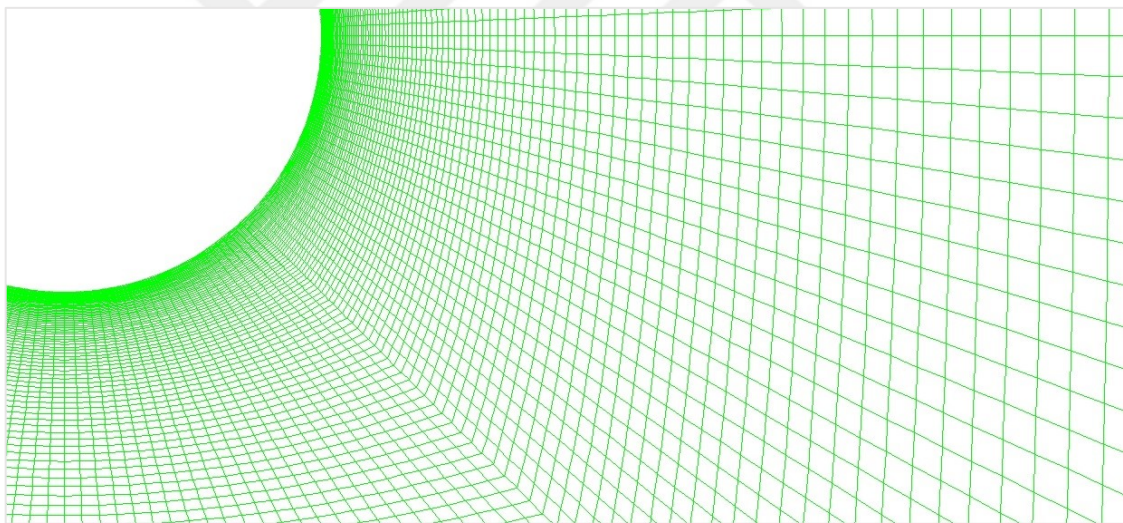


**Figure 4.3** Mesh structure applied to the cylinder

The left and right sides of the computational domain are defined as velocity inlet and pressure outlet respectively. Upper and lower walls are defined as symmetry wall.

#### **4.2 Mesh Independence Study**

To assess the adequacy of mesh, a mesh independence study is done with fixed cylinder case and compared with each other. The grid size is selected that the grid size has no longer affects the results in terms of  $C_D$  and  $C_L$ .

Mesh independence studies are conducted as transient turbulence flow with  $Re=10^4$  with four different grid sizes. As inlet condition, velocity is chosen as  $U=1$  m/s. Cylinder diameter is chosen as  $D=1$  m. Other parameters are calculated so that the  $Re=10^4$  is maintained. Turbulence model is chosen as SST  $k-\omega$ . The pressure-velocity coupling is PISO and the all spatial and the temporal discretization scheme are chosen as second-order upwind scheme. For gradient discretization method, least squares cell-based scheme is chosen.

Turbulence parameters are chosen as  $k=0.001$   $m^2/s^2$  and  $\omega=1$   $1/s$  as in study by Guilmineau and Queutey (Guilmineau and Queutey, 2004). Time step  $\Delta t= 0.005$  s is set to maintain Courant number around 1. For convergence criteria all residuals are set to  $10^{-4}$ .

Table 4.1 shows the comparison of mean  $C_D$ ,  $C_{D, \text{mean}}$ , and the root mean square of  $C_L$ ,  $C_{L, \text{rms}}$ , results with different grid size and the previous studies.

**Table 4.1** Comparison of different grid size

	$C_{D, \text{mean}}$	$C_{L, \text{rms}}$
24300 Cells	1.30	0.95
31400 Cells	1.54	1.13
39300 Cells	1.64	1.23
48000 Cells	1.64	1.23
Gopalkrishnan (1993) Experimental	1.19	-
Norberg (2003) Experimental	-	0.25-0.46

As it is indicated in Table 4.1 using the higher number of cells than 39300, grid size does not affect the results (The difference is smaller than %1). Therefore, all of the following simulations are done with grid with 39300 number of cells.

### **4.3 Validation of 1DOF VIV Simulation**

In this section, the validation process is shown. The CFD simulations are performed for validation of the simulation setup and the comparison of the results with previous studies found in the open literature is shown.

#### **4.3.1 Simulation Setup**

For validation, the study of Khalak and Williamson (Khalak and Williamson, 1996) is chosen and the results are compared with their experimental data and numerical results by Pan et al. (Pan et al., 2007) with the same experimental data as Khalak and Williamson (Khalak and Williamson, 1996). The simulations are in the range of  $3 \leq U_r \leq 13$  with corresponding Reynolds number from 2500 to 10830. The mass damping-ratio is chosen as  $m^* \zeta = 0.0013$  and the mass ratio is chosen as  $m^* = 2.4$  same as the experiments. For simplicity, free-stream velocity  $U = 1$  m/s and mass of the cylinder  $m = 1$  kg is taken. The added mass of the cylinder is calculated as in still water. From Equation 2.13 fluid density is calculated as  $\rho = 0.53$  kg/m<sup>3</sup> and cylinder diameter is chosen as  $D = 1$  m. Natural frequency of the system is calculated as it is in water with added mass. All the other parameters are determined from the dimensionless parameter equations in section 2.6 in order to maintain these values. Table 4.2 summarizes the parameters that are used in the validation process.

Turbulence parameters are chosen as  $k = 0.001$  m<sup>2</sup>/s<sup>2</sup> and  $\omega = 1$  1/s as in study by Guilmineau and Queutey (Guilmineau and Queutey, 2004). Time step  $\Delta t = 0.005$  s is set to maintain Courant number around 1. For convergence criteria all residuals are set to  $10^{-4}$ .

As previously mentioned, turbulence model is chosen as SST  $k-\omega$ . The pressure-velocity coupling is PISO and the all spatial and the temporal discretization scheme is chosen as second-order upwind scheme. For gradient discretization method, least squares cell base scheme is chosen.

For dynamic mesh implementation, ANSYS FLUENT's 6DOF solver is used with diffusion based smoothing method. A user defined function (UDF) is used to define physical properties of cylinder ( $k_s$ ,  $c$  and  $m$ ) and the net force action on system.

**Table 4.2** Simulation parameters for validation

<b>Ur</b>	<b>Re</b>	<b>f<sub>n</sub> (Hz)</b>	<b>k<sub>s</sub> (N/m)</b>	<b>c (N.s/m)</b>	<b>μ (kg/m.s)</b>
3	2500	0.333	6.214	0.0321	2.12x10 <sup>-4</sup>
4	3332	0.250	3.495	0.0241	1.59x10 <sup>-4</sup>
5	4165	0.200	2.237	0.0193	1.27x10 <sup>-4</sup>
6	4998	0.167	1.553	0.0161	1.06x10 <sup>-4</sup>
7	5831	0.143	1.141	0.0138	9.11x10 <sup>-5</sup>
8	6664	0.125	0.874	0.0120	7.97x10 <sup>-5</sup>
9	7497	0.111	0.690	0.0107	7.08x10 <sup>-5</sup>
10	8330	0.100	0.559	0.0096	6.37x10 <sup>-5</sup>
11	9163	0.091	0.462	0.0088	5.80x10 <sup>-5</sup>
12	9996	0.083	0.388	0.0080	5.31x10 <sup>-5</sup>
13	10830	0.077	0.331	0.0074	4.90x10 <sup>-5</sup>

## 4.3.2 Results

### 4.3.2.1 Amplitude Ratio

Figure 4.4 shows the dimensionless amplitude ratio,  $A^*=A/D$ , as a function of corresponding reduced velocity,  $Ur$ , with comparison of experimental data (Khalak and Williamson, 1996) and the numerical results (Pan et al., 2007). Numerical and experimental studies were also done with the mass damping-ratio  $m^*\zeta=0.0013$  and

the mass ratio  $m^*=2.4$ . Although the general trend is captured well, it can be seen that there is an early increase in amplitude during the initial branch while the upper branch is not well captured. This behavior is also reported by both Guilmineau and Queutey (Guilmineau and Queutey, 2004) and Pan et al. (Pan et al., 2007). The reason is URANS method can not capture the randomness of the VIV in upper branch due to its averaging algorithm.

The highest amplitude ratio  $A^*=0.67$  is captured when  $Ur=5$ . Region  $5 < Ur < 12$  corresponds the lock-in region as in the experiments. For  $Ur > 11$  sudden decreases are observed that corresponds to desynchronization region. As it is shown, aside from the upper branch, simulations are in good agreement with both numerical and experimental data.

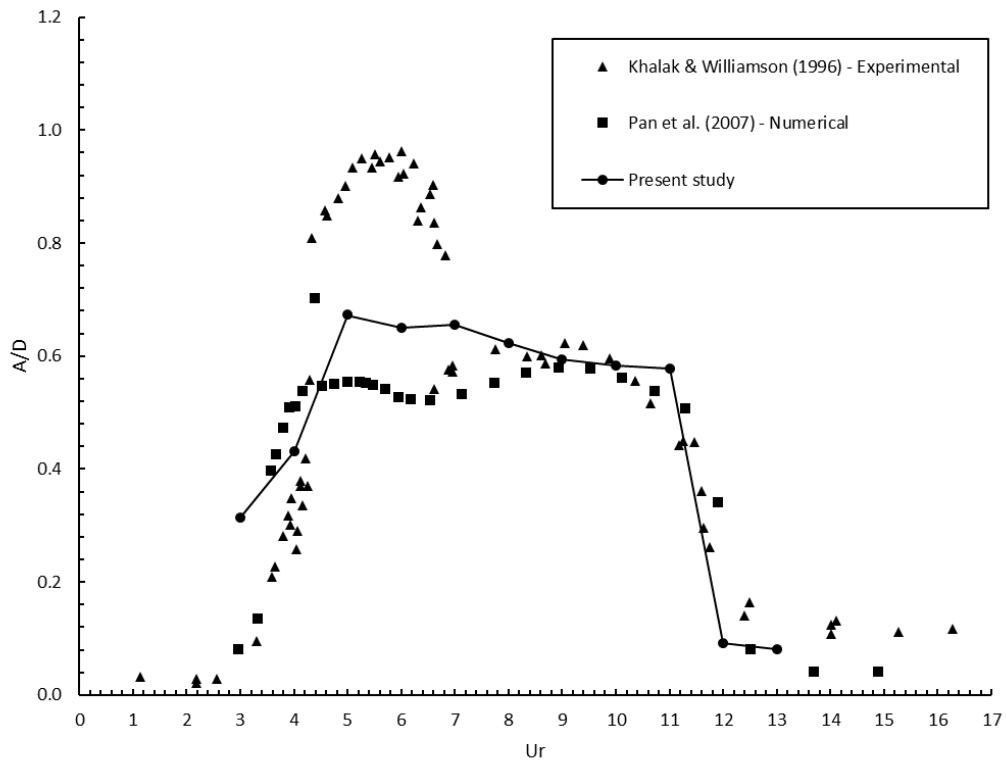


**Figure 4.4** Amplitude ratio,  $A^*$ , as a function of reduced velocity,  $Ur$

#### 4.3.2.2 Drag and Lift Coefficients

Figure 4.5, Figure 4.6, Figure 4.7 and Figure 4.8 shows the time trace of dimensionless parameters (Dimensionless amplitude,  $A^*=A/D$ , lift coefficient,  $C_L$  and drag coefficient,  $C_D$ ). During initial branch ( $Ur < 5$ ), beating phenomenon is

observed and the oscillation is not fully sinusoidal, this can be also observed from the spectral density graphs, since there are two fundamental frequencies while the system is in the initial branch. One of them is shedding frequency other one is due to system's natural frequency.

During lock-in region ( $5 < U_r < 12$ ),  $C_D$  increases dramatically in the beginning of the lock-in region and decreases with the increased  $U_r$ . After desynchronizing,  $C_D$  decreases to a mean around 1.05. However, lift coefficient decreases in the beginning of the lock-in region and continues to decrease as the  $U_r$  increases throughout lock-in region. As a summary, in Figure 4.9 the highest force coefficients that is recorded, rms of  $C_L$  and mean  $C_D$  are presented. Similar trend is observed by both Guilmineau and Queutey (Guilmineau and Queutey, 2004) and Pan et al. (Pan et al., 2007).

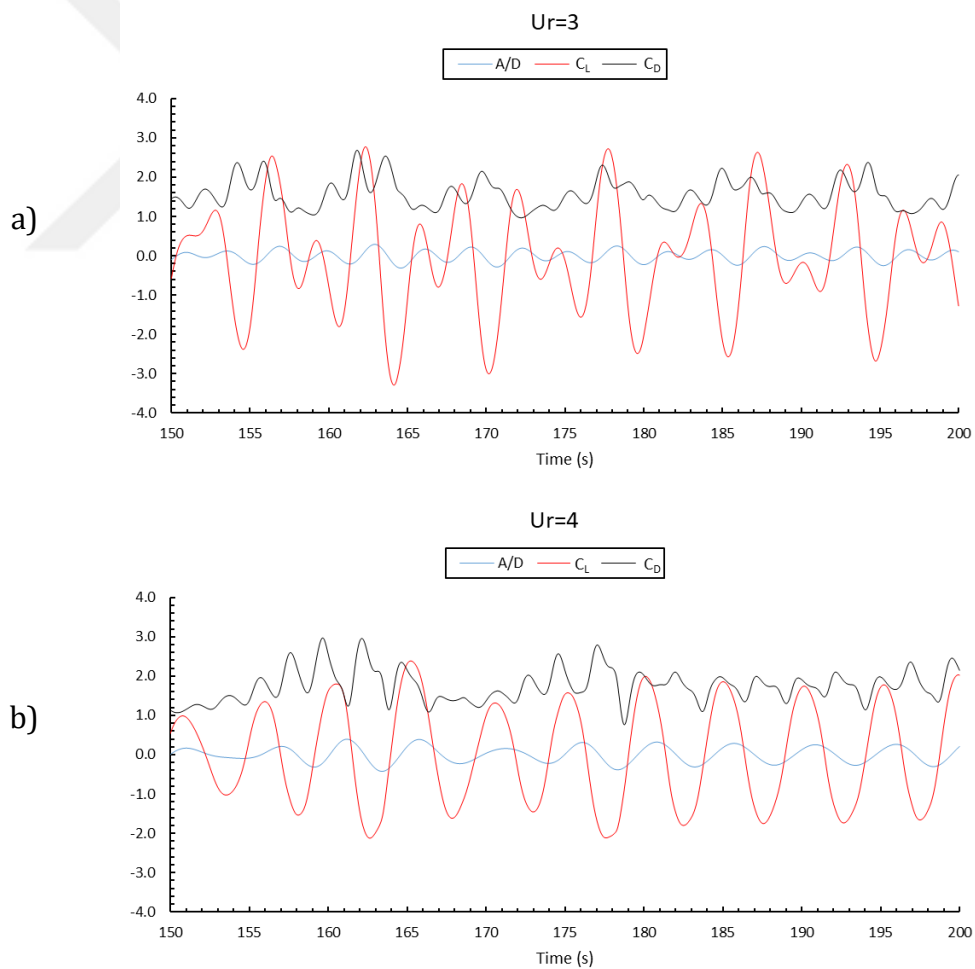


**Figure 4.5** Time trace of  $A^*$ ,  $C_L$  and  $C_D$  for a)  $U_r=3$  and b)  $U_r=4$

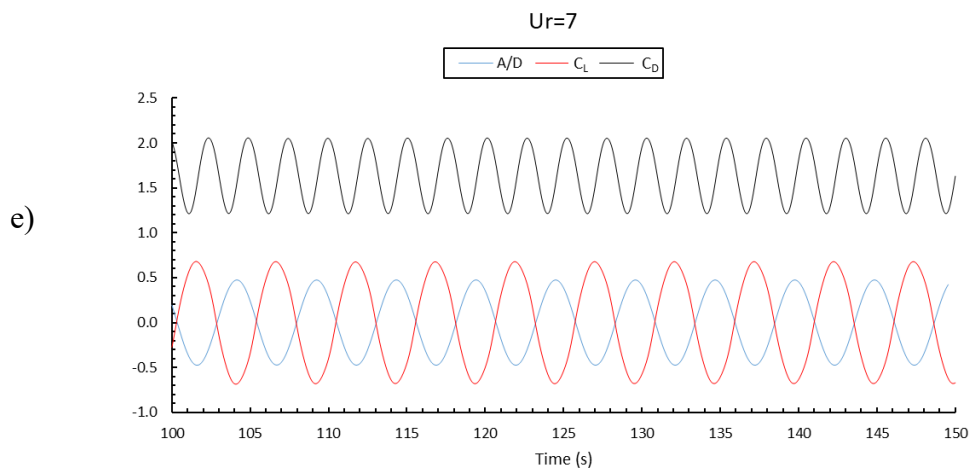
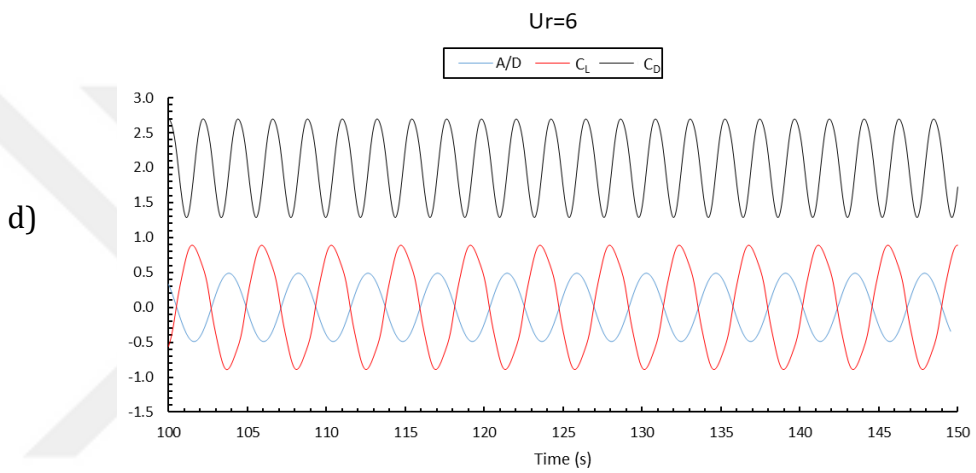
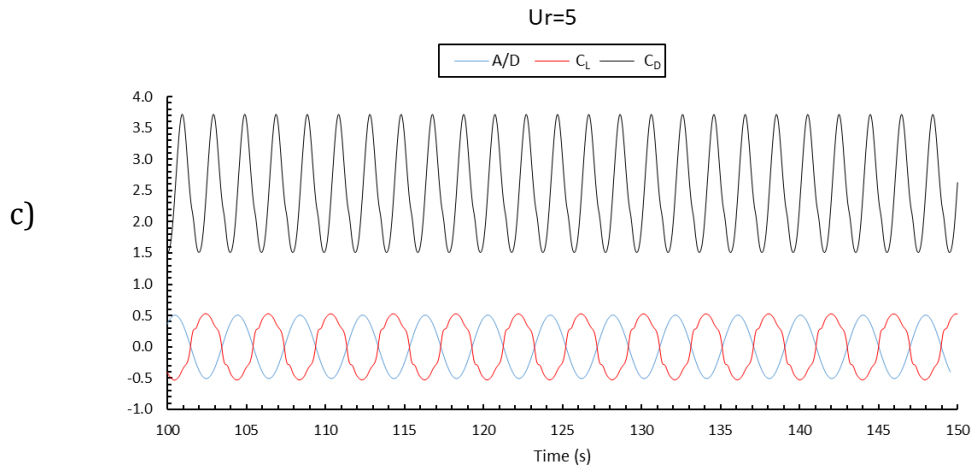


**Figure 4.6** Time trace of  $A^*$ ,  $C_L$  and  $C_D$  for c)  $Ur=5$ , d)  $Ur=6$  and e)  $Ur=7$

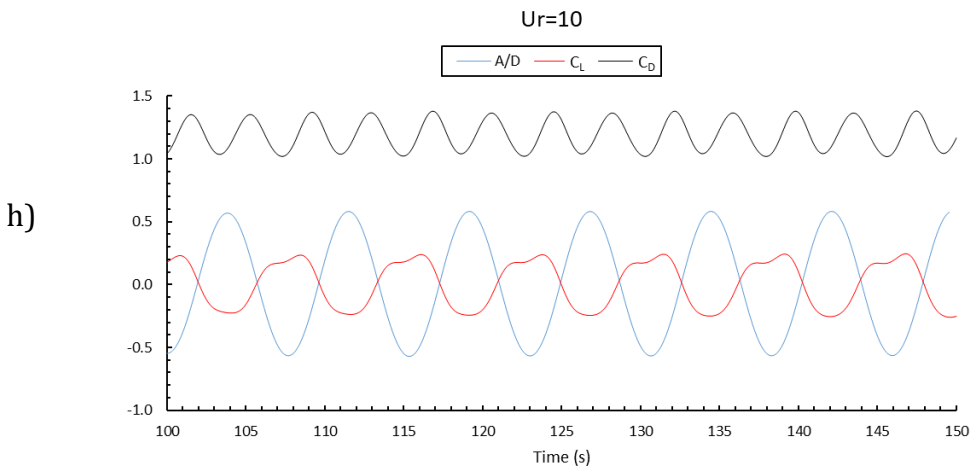
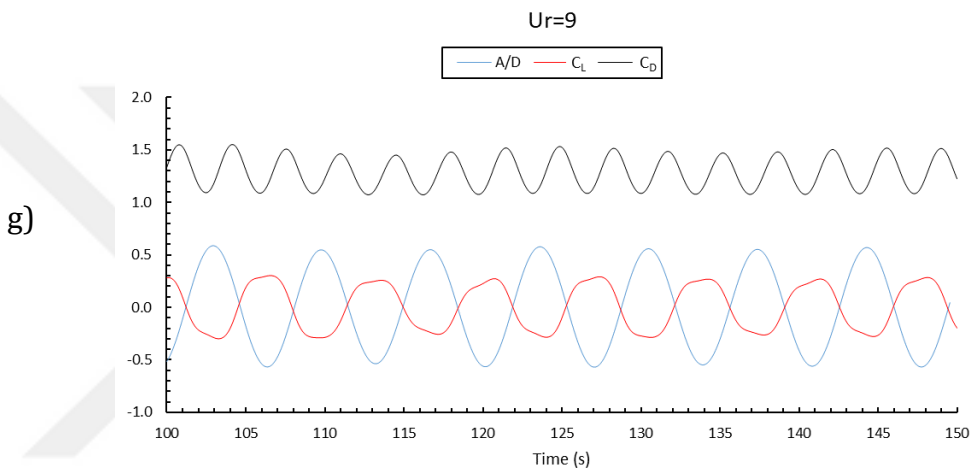
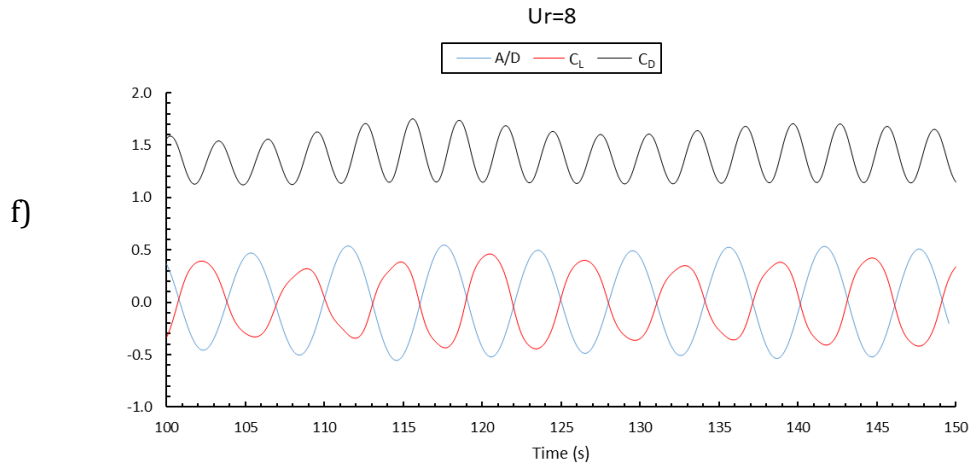


**Figure 4.7** Time trace of  $A^*$ ,  $C_L$  and  $C_D$  for f)  $Ur=8$ , g)  $Ur=9$  and h)  $Ur=10$

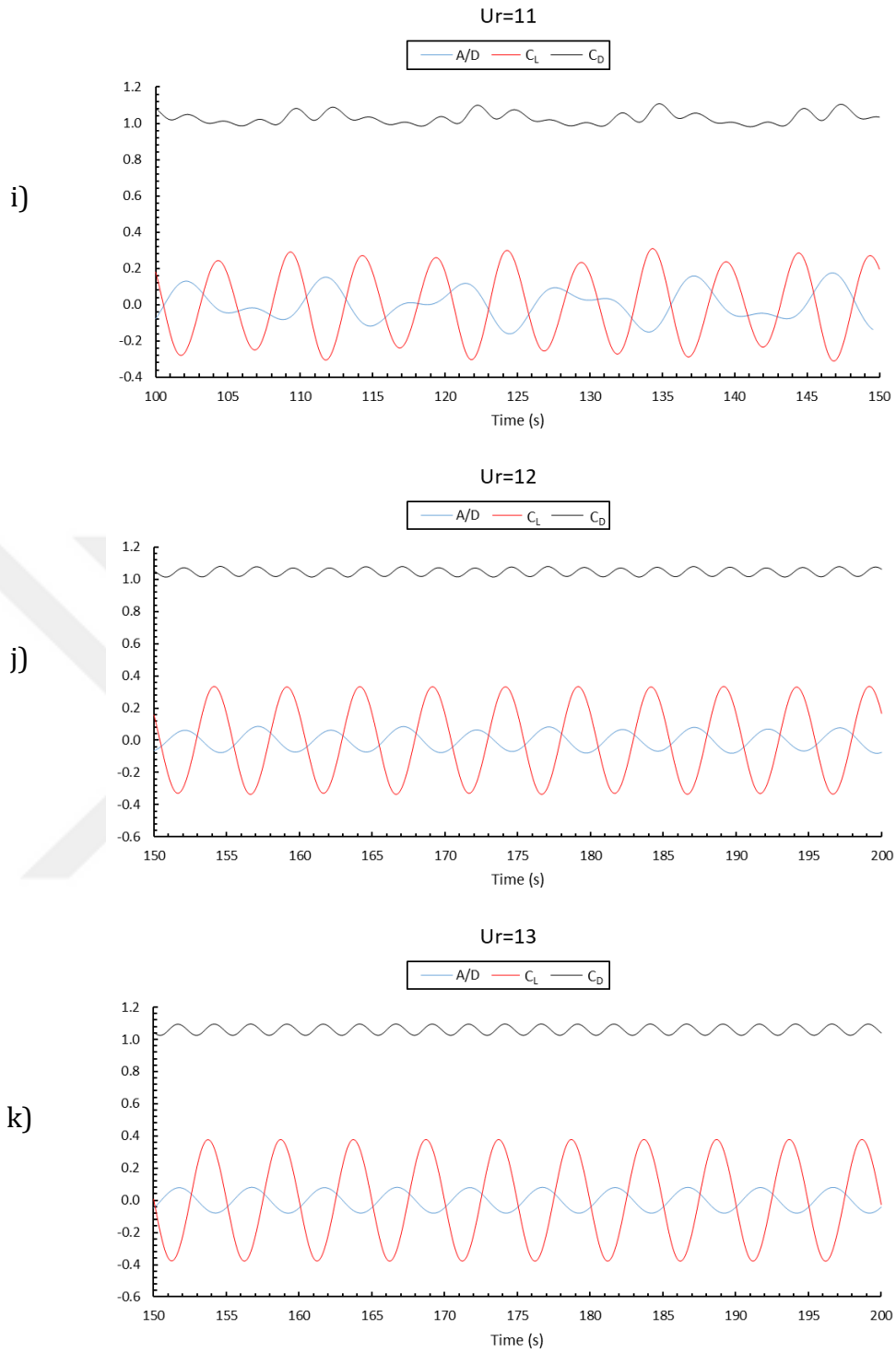


**Figure 4.8** Time trace of  $A^*$ ,  $C_L$  and  $C_D$  for i)  $Ur=11$ , j)  $Ur=12$  and k)  $Ur=13$

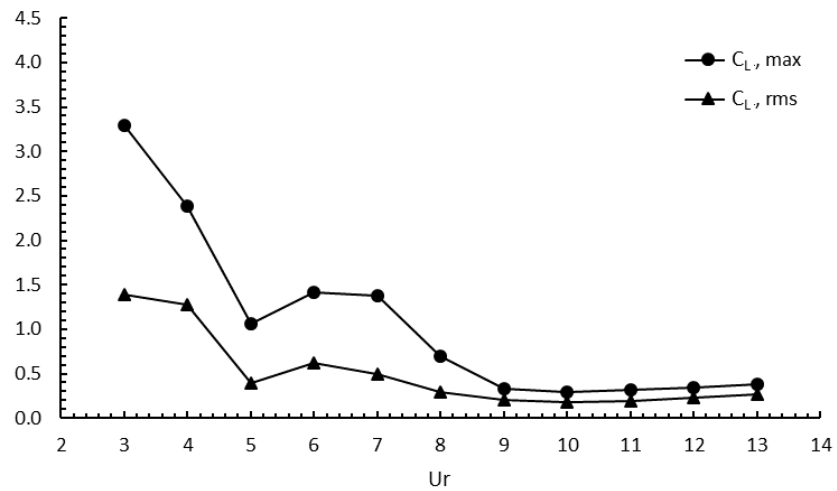
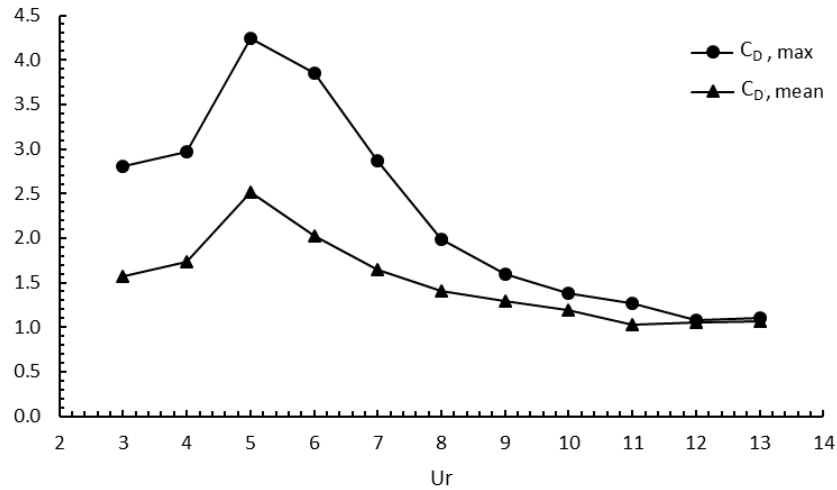


**Figure 4.9** Summary of force coefficients in terms of  $C_D$  max,  $C_D$  mean,  $C_L$  max and  $C_L$  rms as function of corresponding  $Ur$

#### 4.3.2.3 Frequency Ratio and Phase Angle

The frequency ratio  $f^*$  is obtained as shown in Figure 4.10 as a function of corresponding  $Ur$ . Also, Figure 4.11 and Figure 4.12 shows the spectral density of displacement of the cylinder. Initial branch consists of two frequencies; one of them is shedding frequency other one is system's natural frequency. During lock-in region, only one dominant frequency occurs, as can be seen in the spectral density graph of displacement (Figure 4.11 and Figure 4.12). While system is in lock-in region the  $f^*$  is around 1.3. This is an indication that the simulations are in good agreement with both experimental and numerical results, especially in the lower branch. Within both initial branch and desynchronizing, the fundamental frequency

ratios are about in-line with the Strouhal line  $f_{st}$ , which is the ratio of  $U_r$  over Strouhal number (Strouhal number is nearly 0.2 throughout all Reynolds numbers in this study). This is also a clear indication that system is not in the lock-in state.

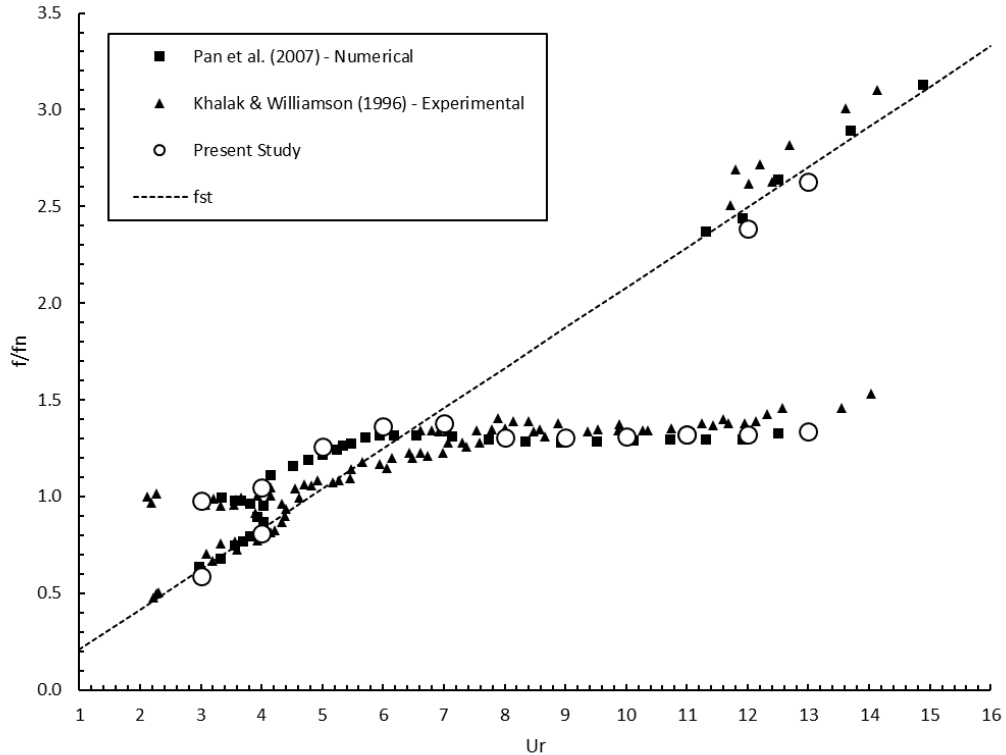


**Figure 4.10** Frequency ratio  $f^*$  as a function of corresponding  $U_r$

The phase angle,  $\phi$ , is shown in Figure 4.13 as a function of  $U_r$ . It is calculated from Equation 2.19. It is observed that, during initial branch, the fluid forces and the displacement of the system are in phase. After  $U_r=5$ , a sudden change in  $\phi$  occurs that is an indication of fluid forces and the displacement is no longer in phase and the lock-in occurs. Overall, the results are in good agreement with the previous numerical study by Pan et al. (Pan et al., 2007).

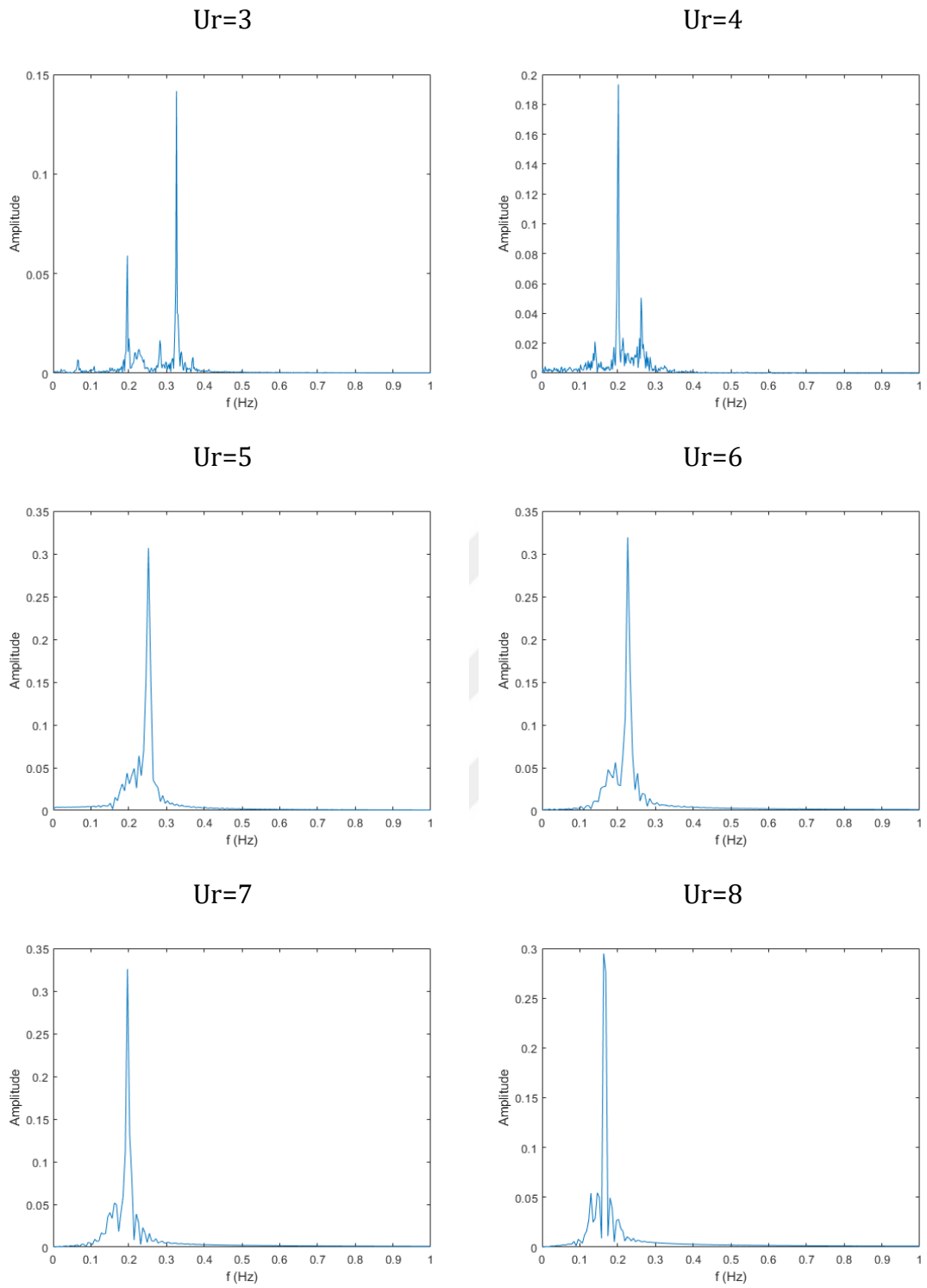


**Figure 4.11** Spectral density of displacement of corresponding  $U_r$

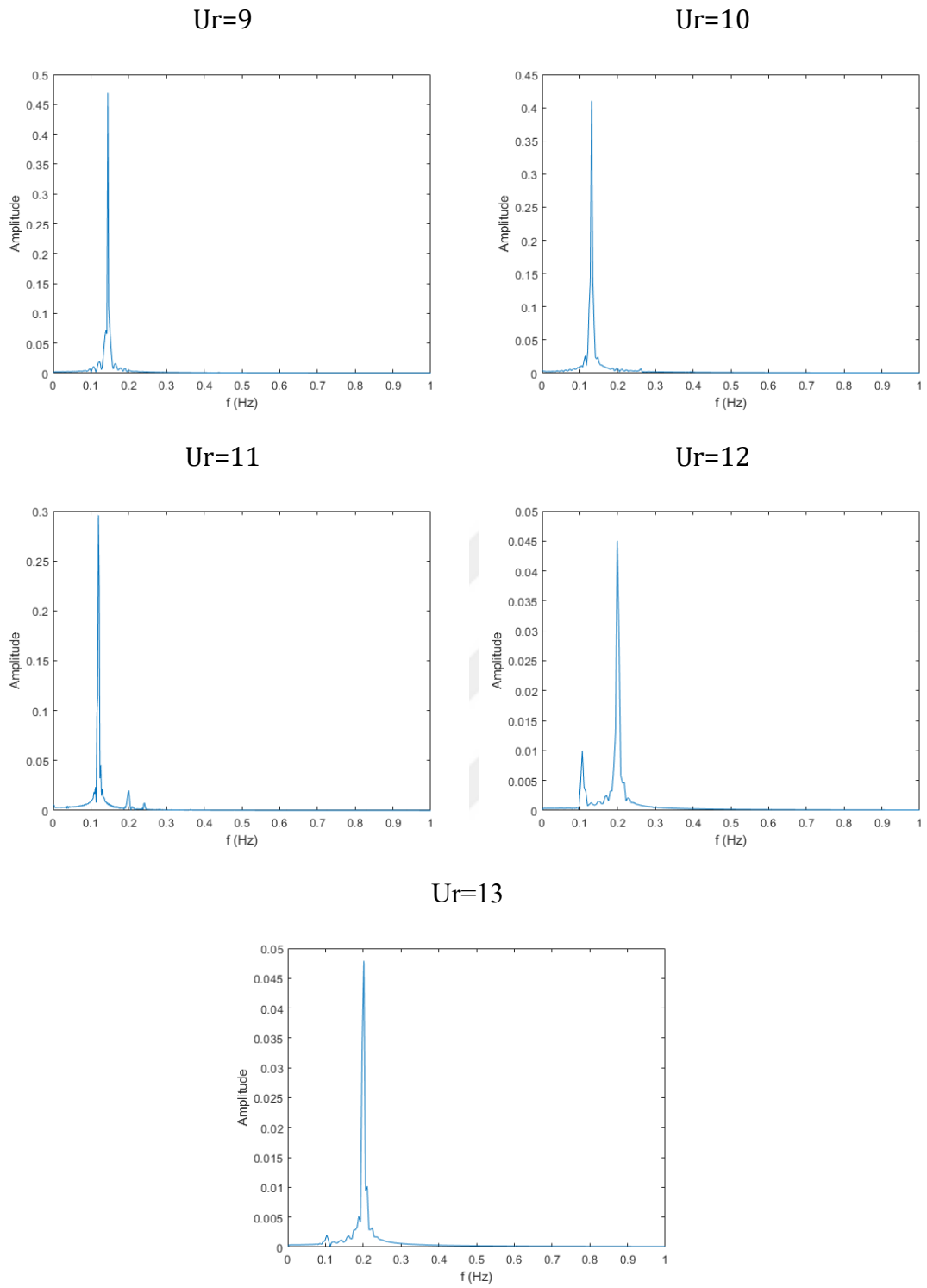


**Figure 4.12** Spectral density of displacement of corresponding  $U_r$

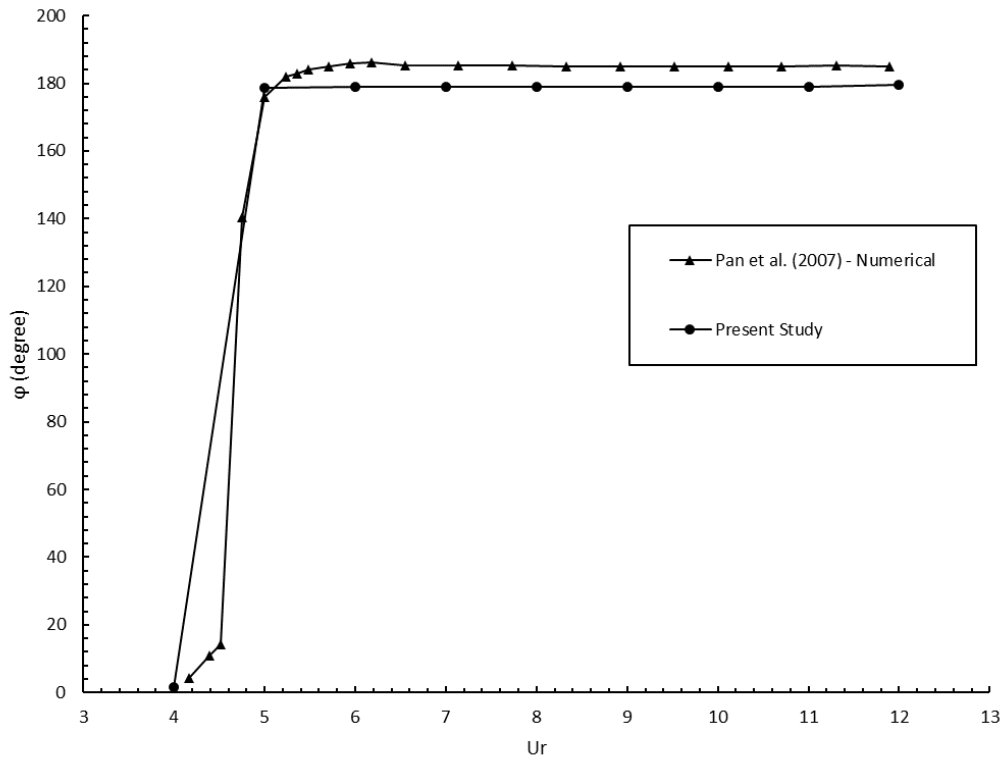


**Figure 4.13** Phase angle,  $\phi$ , as a function of corresponding  $Ur$

#### 4.3.2.4 Vortex Formation Modes

One of the most important indications of branch transition is the change in vortex mode in the wake region. Figure 4.14 shows vorticity contours of corresponding  $Ur$ .  $Ur=4$  corresponds to 2S mode as an indication of initial branch. In 2S mode, Wake occurs as two single vortices per cycle. When lock-in happens, 2P vortex mode occurs as an indication of lock-in. Both,  $Ur=5$  and  $Ur=8$  vortex formation vortices form as a 2P mode. In 2P mode wake region has two pair of vortices per cycle. These results are in good accordance with both numerical (Pan et al., 2007) and experimental study (Govardhan and Williamson, 1999).

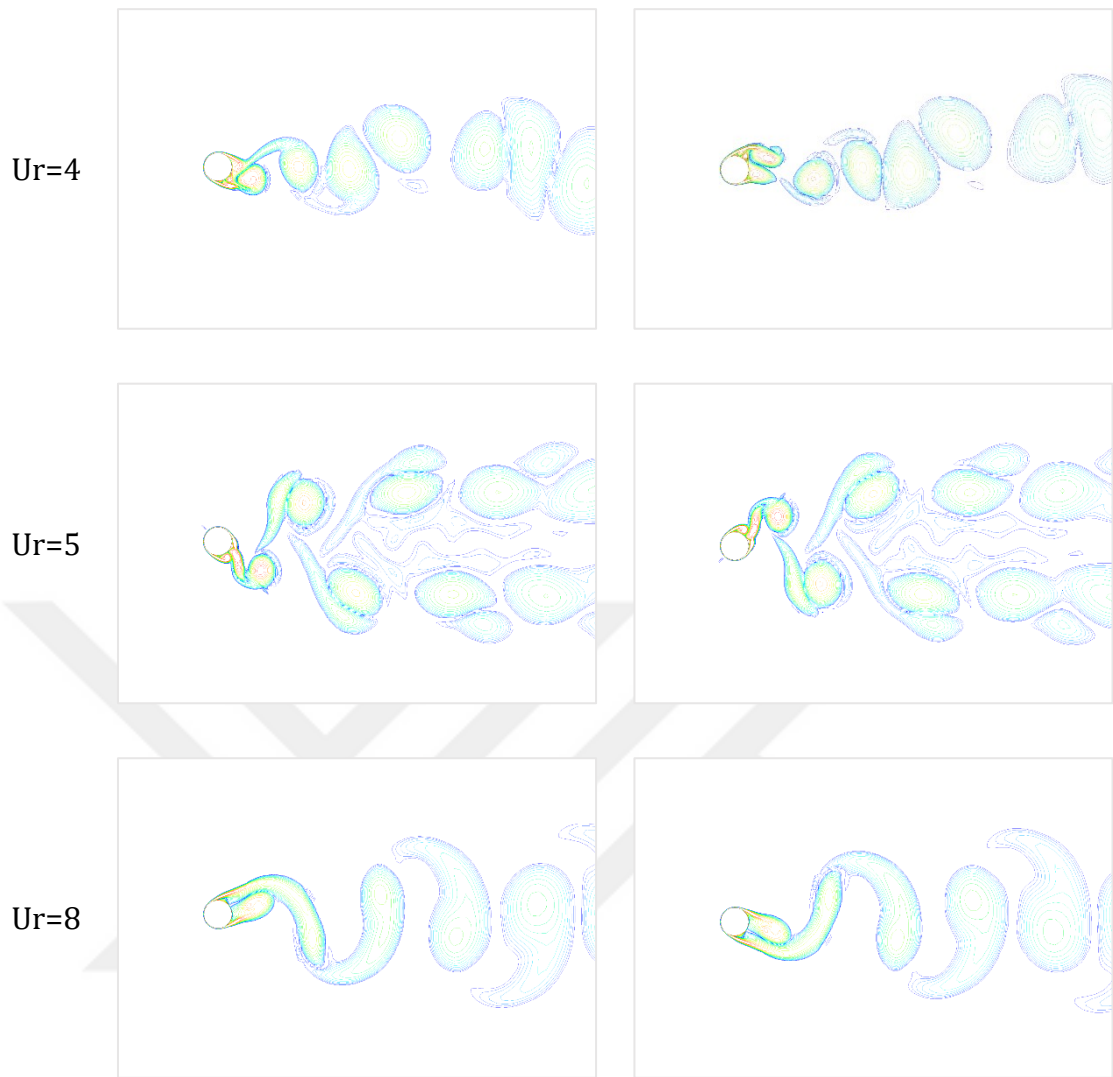


**Figure 4.14** Vortex modes of  $Ur=4$  (2S),  $Ur=5$  (2P) and  $Ur=8$  (2P)

## 1DOF Vortex-Induced Vibration with Different Damping Parameters

---

This section describes the simulation of 1DOF vortex-induced vibration in transverse direction with different damping parameters. Simulations are done with damping  $\zeta = 0.028$  and  $\zeta = 0.074$ . Mass ratio  $m^*$  is taken as 3 as in the experimental study by Soti et al. (Soti et al., 2018). The simulations are in the range of  $3.6 \leq Ur \leq 12$  with corresponding Reynolds number from 2220 to 6661. The results are presented and compared with experimental data by Soti et al. (Soti et al., 2018).

### 5.1 Numerical Setup

For simplicity, free-stream velocity  $U=1$  m/s and mass of the cylinder  $m=1$  kg are chosen. From Equation 2.13 fluid density is calculated as  $\rho=0.42$  kg/m<sup>3</sup>. The added mass of the cylinder is calculated as in still water. Natural frequency of the system is calculated as it is in water with added mass. All the other parameters are determined from the dimensionless parameter equations in Section 2.6 in order to maintain these values. Table 5.1 summarizes the parameters that are used in the simulations. As previously mentioned, cylinder diameter is taken as  $D=1$  m.

Turbulence parameters are chosen as  $k=0.001$  m<sup>2</sup>/s<sup>2</sup> and  $\omega=1$  1/s as in study by Guilmineau and Queutey (Guilmineau and Queutey, 2004). Time step  $\Delta t= 0.005$  s is set to maintain Courant number,  $C$ , around 1. For convergence criteria all residuals are set to  $10^{-4}$ .

As previously mentioned, turbulence model is chosen as SST  $k-\omega$ . The pressure-velocity coupling is PISO and the all spatial and the temporal discretization scheme are chosen as second-order upwind scheme. For gradient discretization method, least squares cell base scheme is chosen.

For dynamic mesh implementation, ANSYS FLUENT's 6DOF solver is used with diffusion based smoothing method. A user defined function (UDF) is used to define physical properties of cylinder ( $k_s$ ,  $c$  and  $m$ ) and the net force acting on system.

**Table 5.1** Simulation parameters for  $\zeta = 0.028$  and  $\zeta = 0.074$

Ur	Re	f <sub>n</sub> (Hz)	k <sub>s</sub> (N/m)	c (N.s/m)		μ (kg/m.s)
				ζ = 0.028	ζ = 0.074	
3.6	2221	0.278	4.061	0.1303	0.3443	1.89x10 <sup>-4</sup>
4	2432	0.250	3.289	0.1173	0.3099	1.73x10 <sup>-4</sup>
5	2961	0.200	2.105	0.0938	0.2479	1.42x10 <sup>-4</sup>
6	3490	0.167	1.462	0.0782	0.2066	1.20x10 <sup>-4</sup>
7	4018	0.143	1.074	0.0670	0.1771	1.05x10 <sup>-4</sup>
8	4547	0.125	0.822	0.0586	0.1549	9.24x10 <sup>-5</sup>
9	5075	0.111	0.650	0.0521	0.1377	8.28x10 <sup>-5</sup>
10	5604	0.100	0.526	0.0469	0.1240	7.50x10 <sup>-5</sup>
11	6132	0.091	0.435	0.0426	0.1127	6.85x10 <sup>-5</sup>
12	6661	0.083	0.365	0.0391	0.1033	6.31x10 <sup>-5</sup>

## 5.2 Results for ζ = 0.028

### 5.2.1 Amplitude Ratio

Figure 5.1 shows the dimensionless amplitude ratio,  $A^* = A/D$ , as a function of corresponding reduced velocity  $U_r$  with comparison of experimental data (Soti et al., 2018). Both the simulations and experimental study are done with  $\zeta = 0.028$  and the mass ratio  $m^* = 3$ . From the results, it can be seen that general VIV trend is

captured. However, as in the validation, an early rise in the amplitude is observed. Also, upper branch is not captured well. As previously mentioned, URANS method can not capture the randomness of the VIV in upper branch due to its averaging algorithm. The highest amplitude ratio  $A^*=0.55$  is captured when  $Ur=5$ .

In this study, for  $Ur>8$  a sudden decrease is observed which is the indication of desynchronization. However, experimental data show that desynchronization occurs for  $Ur>11$ . In this study, since all simulations are in 2D domain these results are expected. Previous study by Rahman and Thiagarajan (Rahman and Thiagarajan, 2015), shows the aspect ratio has a great effect on both amplitude and the lock-in region range. The experiments conducted by Soti et al. (Soti et al., 2018) are done with a cylindrical structure that has a  $L/D=20.5$  aspect ratio. Consequently, the lower amplitude ratio and the narrow lock-in region are most likely due to aspect ratio effect.

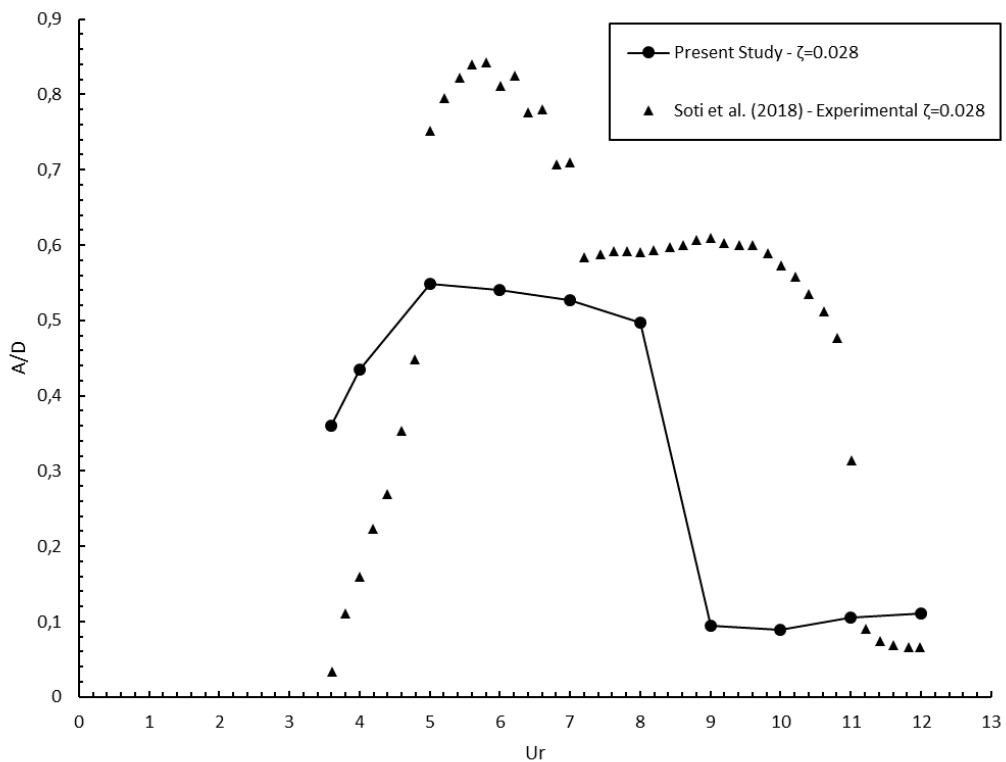


**Figure 5.1** Amplitude ratio,  $A^*$ , as a function of reduced velocity  $Ur$  for  $\zeta=0.028$

## 5.2.2 Drag and Lift Coefficients

Figure 5.2, Figure 5.3, Figure 5.4 and Figure 5.5 shows the time trace of dimensionless parameters (Dimensionless amplitude,  $A^*=A/D$ , lift coefficient,  $C_L$  and drag coefficient,  $C_D$ ).

Similar trend is observed. Results show that during initial branch  $Ur < 5$  beating phenomenon is observed as expected which can be seen from the time trace of force coefficients as they are not fully sinusoidal (Figure 5.2 and Figure 5.3).

For lock-in region ( $5 < Ur < 8$ )  $C_D$  increases dramatically in the beginning of the lock-in region and decreases as  $Ur$  increases. Lift coefficient decreases in the beginning of the lock-in region and continues to decrease as the  $Ur$  increases within lock-in region. With increased damping, relative to validation, it is observed that  $C_{L,rms}$  and  $C_{D,mean}$  are not affected much. However, the highest values of  $C_L$  and  $C_D$  decrease as shown in Figure 5.6.

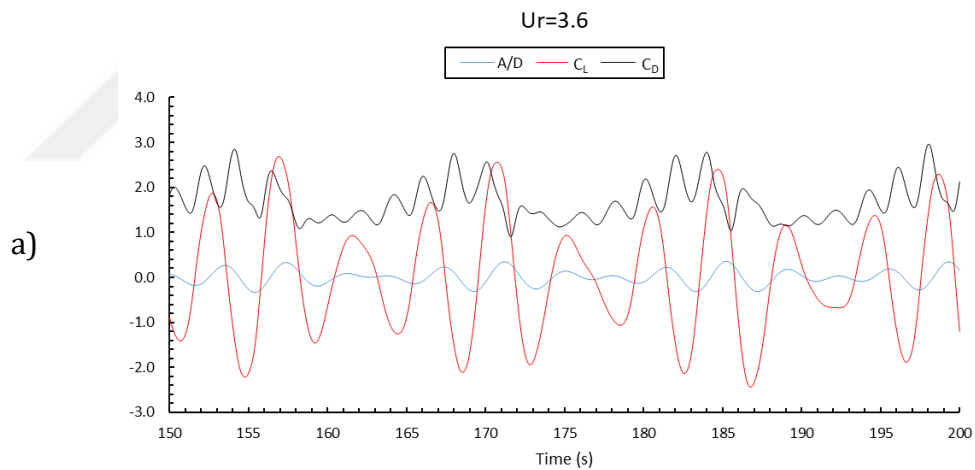


**Figure 5.2** Time trace of  $A^*$ ,  $C_L$  and  $C_D$  for a)  $Ur=3.6$  for  $\zeta = 0.028$

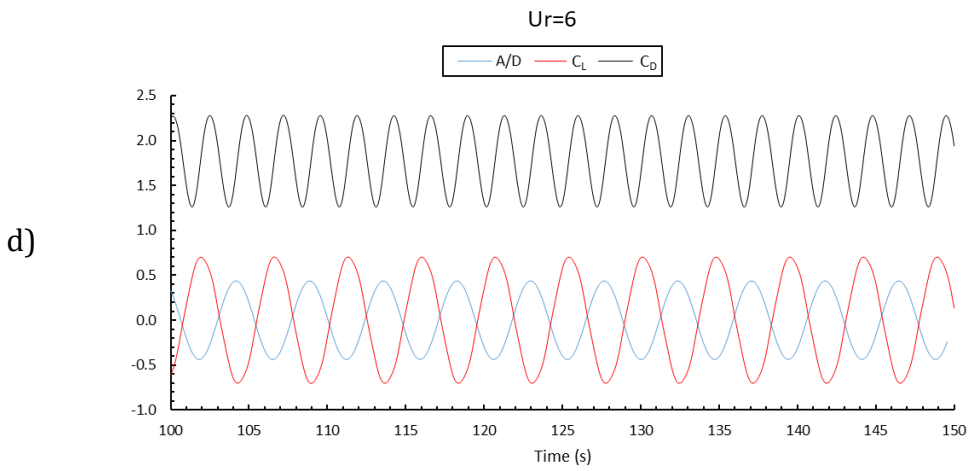
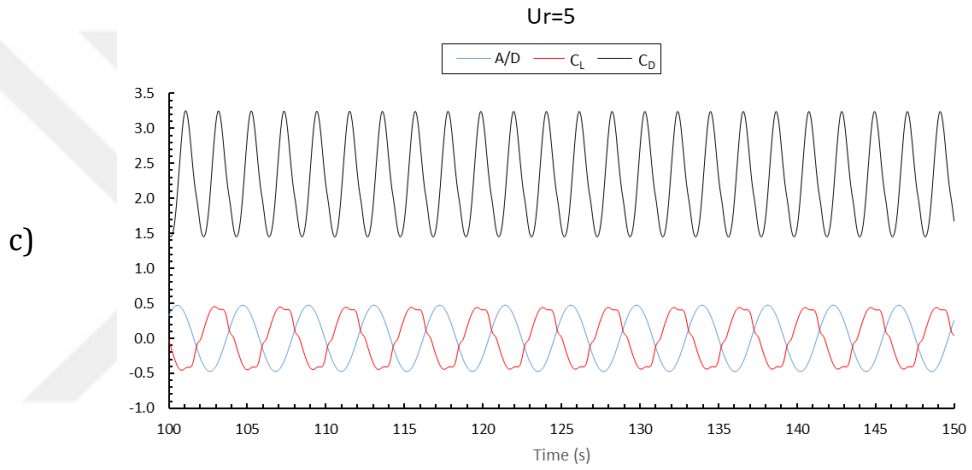
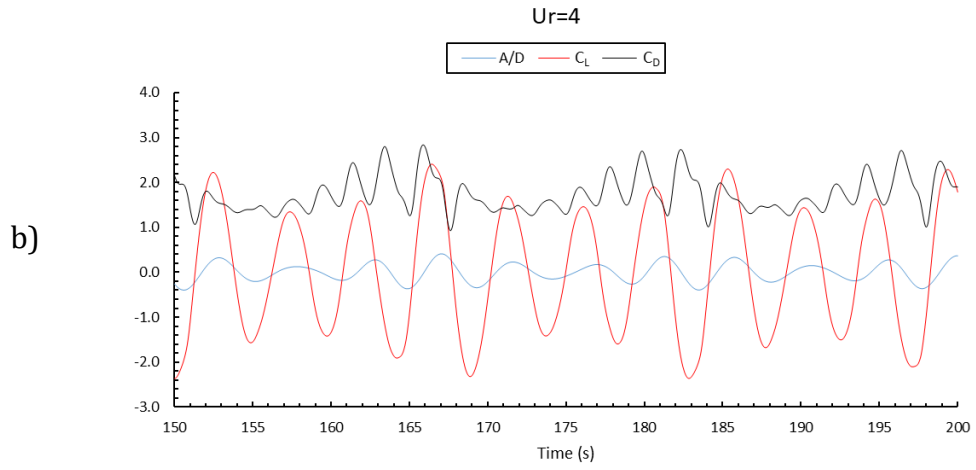


**Figure 5.3** Time trace of  $A^*$ ,  $C_L$  and  $C_D$  for b)  $Ur=4$ , c)  $Ur=5$  and d)  $Ur=6$  for  $\zeta=0.028$

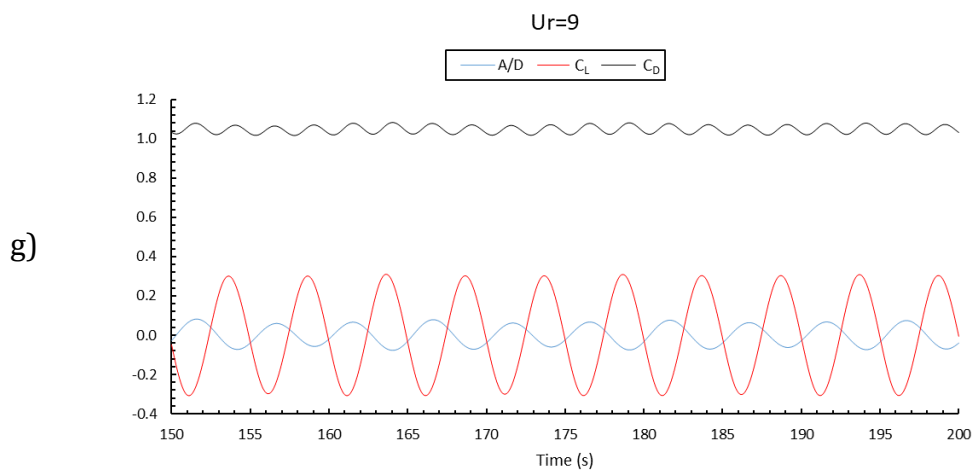
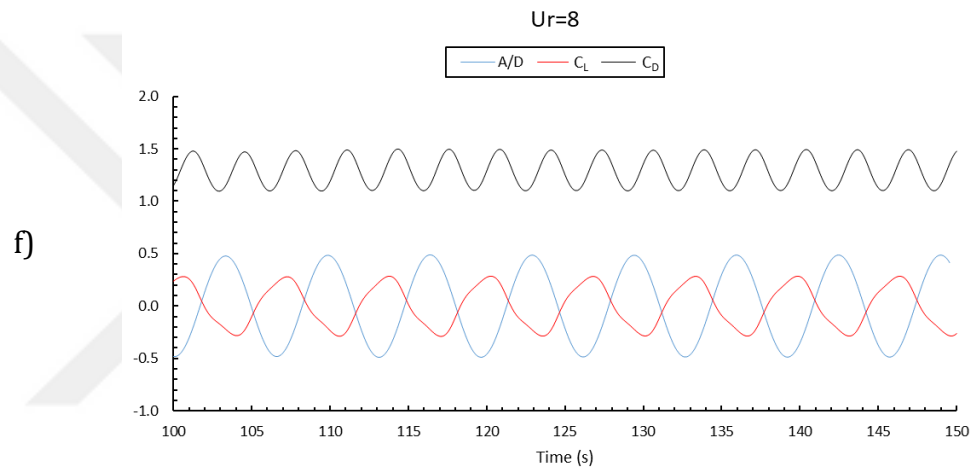
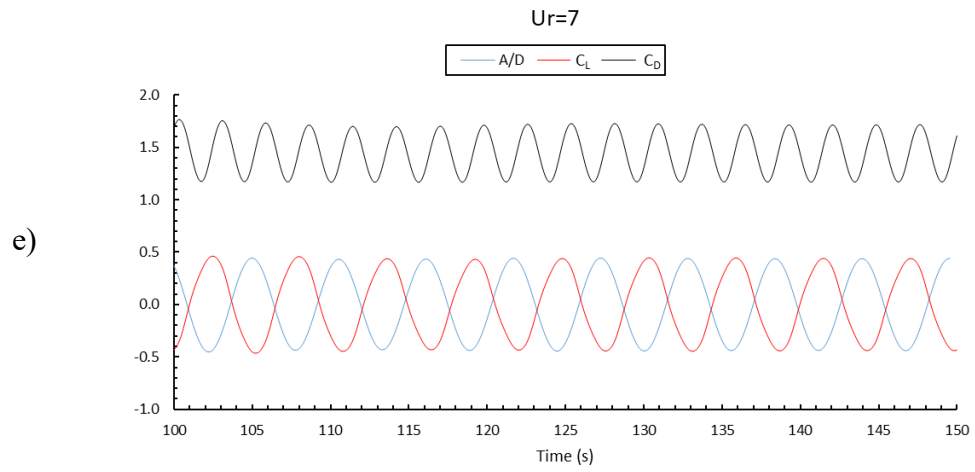


**Figure 5.4** Time trace of  $A^*$ ,  $C_L$  and  $C_D$  for e)  $Ur=7$ , f)  $Ur=8$  and g)  $Ur=9$  for  $\zeta=0.028$

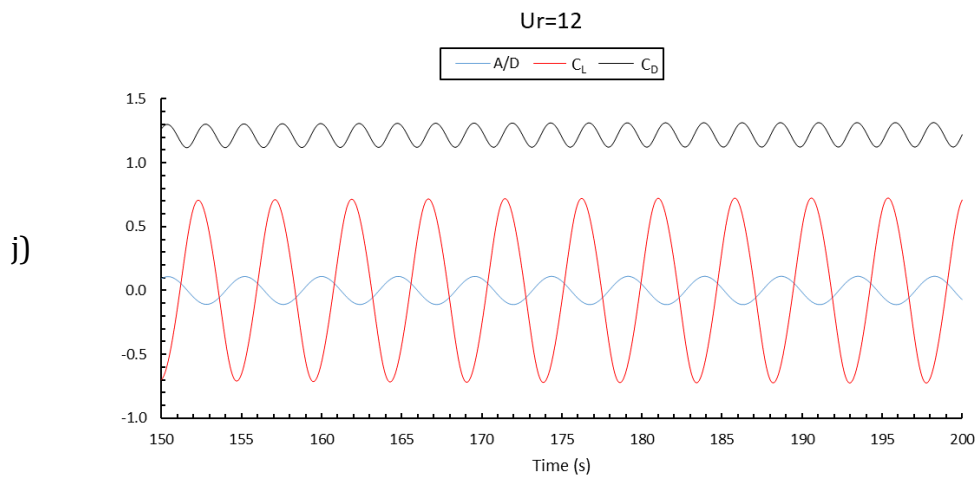
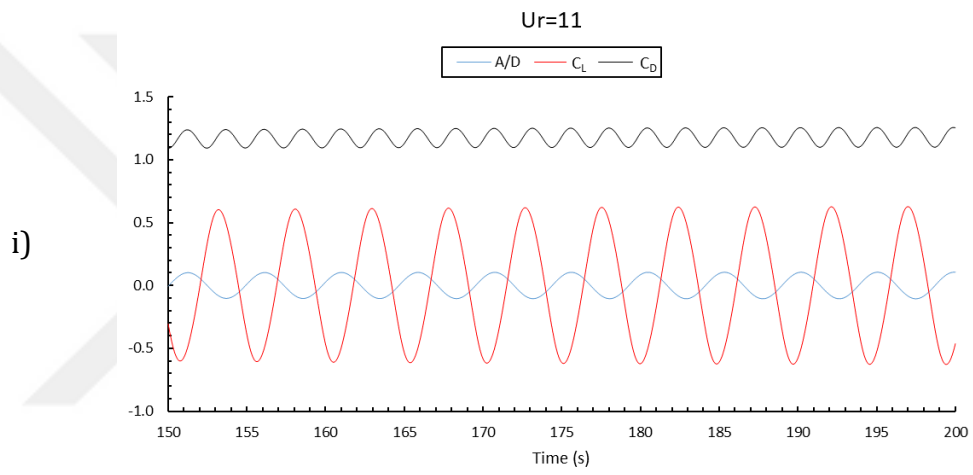
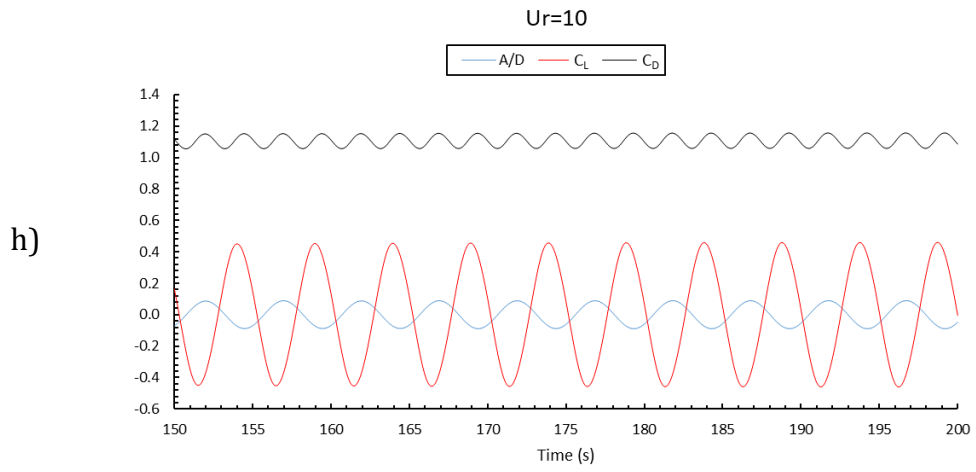


**Figure 5.5** Time trace of  $A^*$ ,  $C_L$  and  $C_D$  for h)  $Ur=10$ , i)  $Ur=11$  and j)  $Ur=12$  for  $\zeta=0.028$

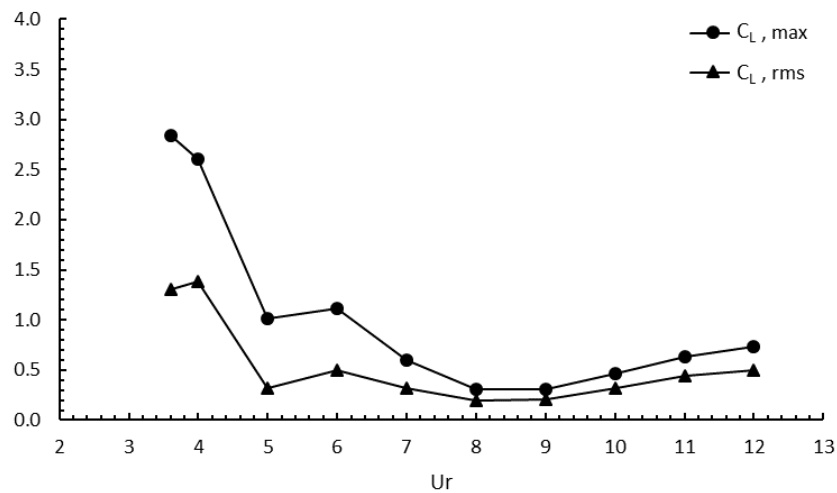
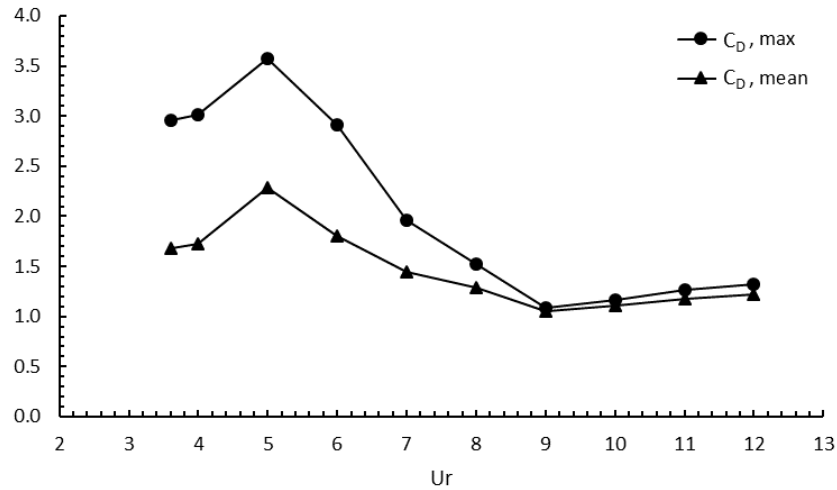


**Figure 5.6** Summary of force coefficients in terms of  $C_D$  max,  $C_D$  mean,  $C_L$  max and  $C_L$  rms as function of corresponding  $Ur$  for  $\zeta=0.028$

### 5.2.3 Frequency Ratio and Phase Angle

The frequency ratio  $f^*$  is shown in Figure 5.7 as a function of corresponding  $Ur$ . Also, the experimental spectral graph (Soti et al., 2018) is shown in the figure for  $\zeta=0.028$ . Figure 5.8 and Figure 5.9 shows the spectral density of the displacement of the cylinder for  $\zeta=0.028$ .

Initial branch consists of two frequencies; one of them is shedding frequency and other one system's natural frequency. When the lock-in happens vortex shedding frequency locked with the natural frequency. Within the lock-in region only one dominant frequency occurs as can be seen in the displacement spectral density graphs (Figure 5.8).

As Figure 5.7 shows, the start of the lock-in can be identifying in small jump in the  $f^*$  at  $Ur=5$ . Since the upper branch that is not captured well in the present work, the frequency ratio in the upper branch region is not captured well neither. However, for initial ( $Ur<5$ ) and lower branch ( $7\leq Ur\leq 8$ ) the present work agrees well with the experimental data. Also, for  $Ur>8$  desynchronization can be clearly observed.

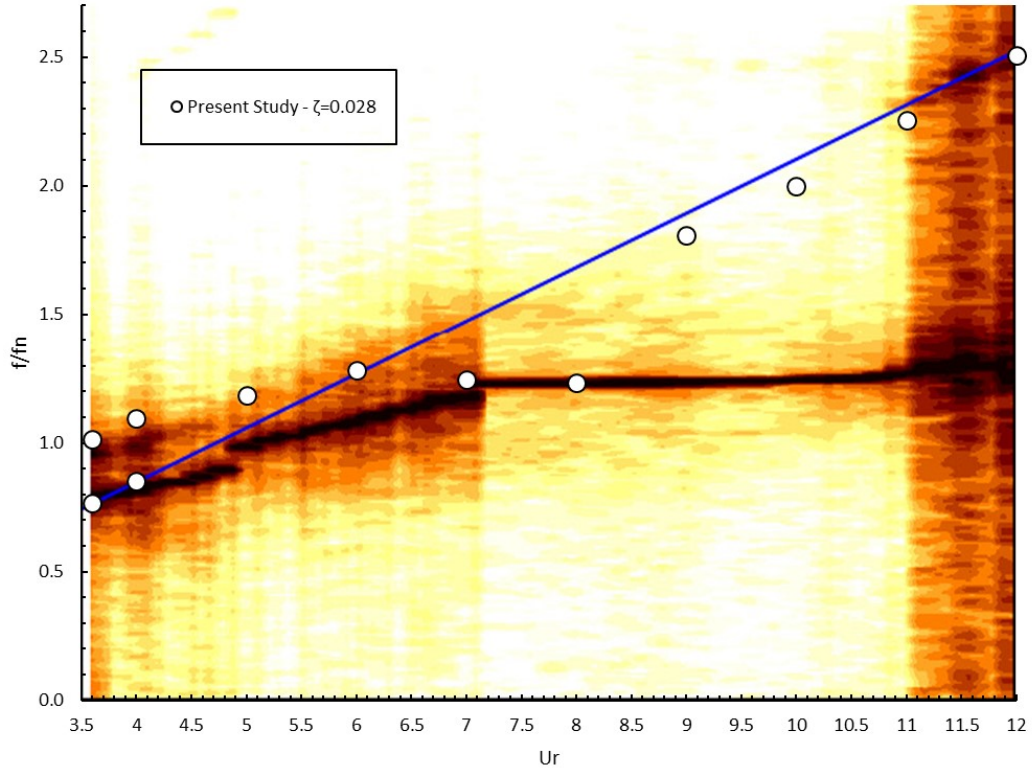


**Figure 5.7** Frequency ratio  $f^*$  as a function of corresponding  $Ur$  for  $\zeta=0.028$

The phase angle,  $\phi$ , is shown in Figure 5.10 as a function of  $Ur$  with the comparison of vortex phase of the experimental data by Soti et al. (Soti et al., 2018). It is calculated from Equation 2.19. According to Soti et al. (Soti et al., 2018), jump in vortex phase is indication of wake change from 2S to 2P mode, means transition from initial branch to lock-in region. As expected, during initial branch, the fluid forces and the displacement are in phase. From the Figure 5.10, initial branch transition can be seen at  $Ur=5$ , as the sudden change in  $\phi$  is happened due to start of lock-in, which means that the fluid forces and the displacement are no longer in phase. However, smooth transition of experimental data is not captured well. Overall, the results are in good agreement with the experimental data.

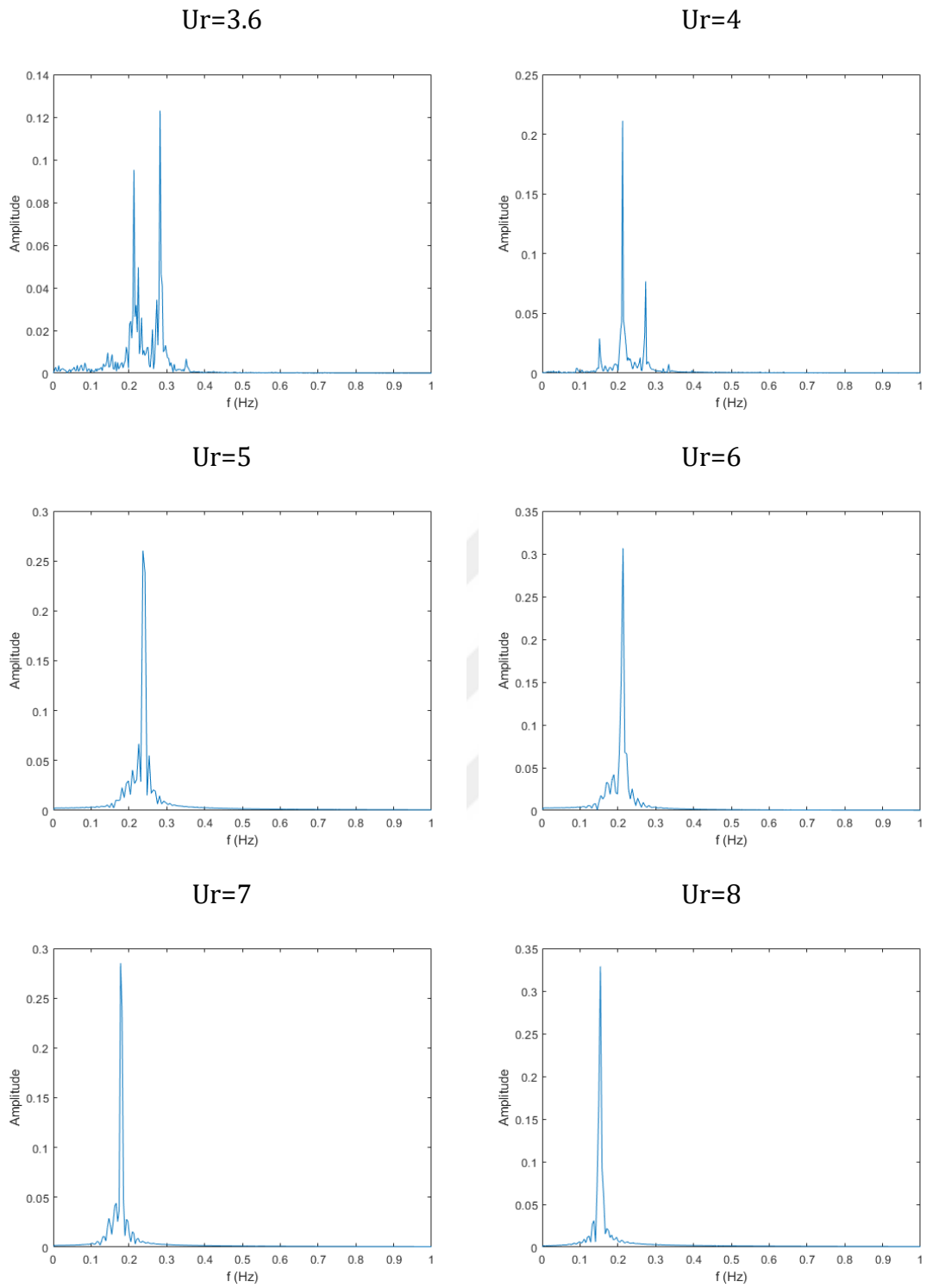


**Figure 5.8** Spectral density of displacement of corresponding  $U_r$  for  $\zeta=0.028$

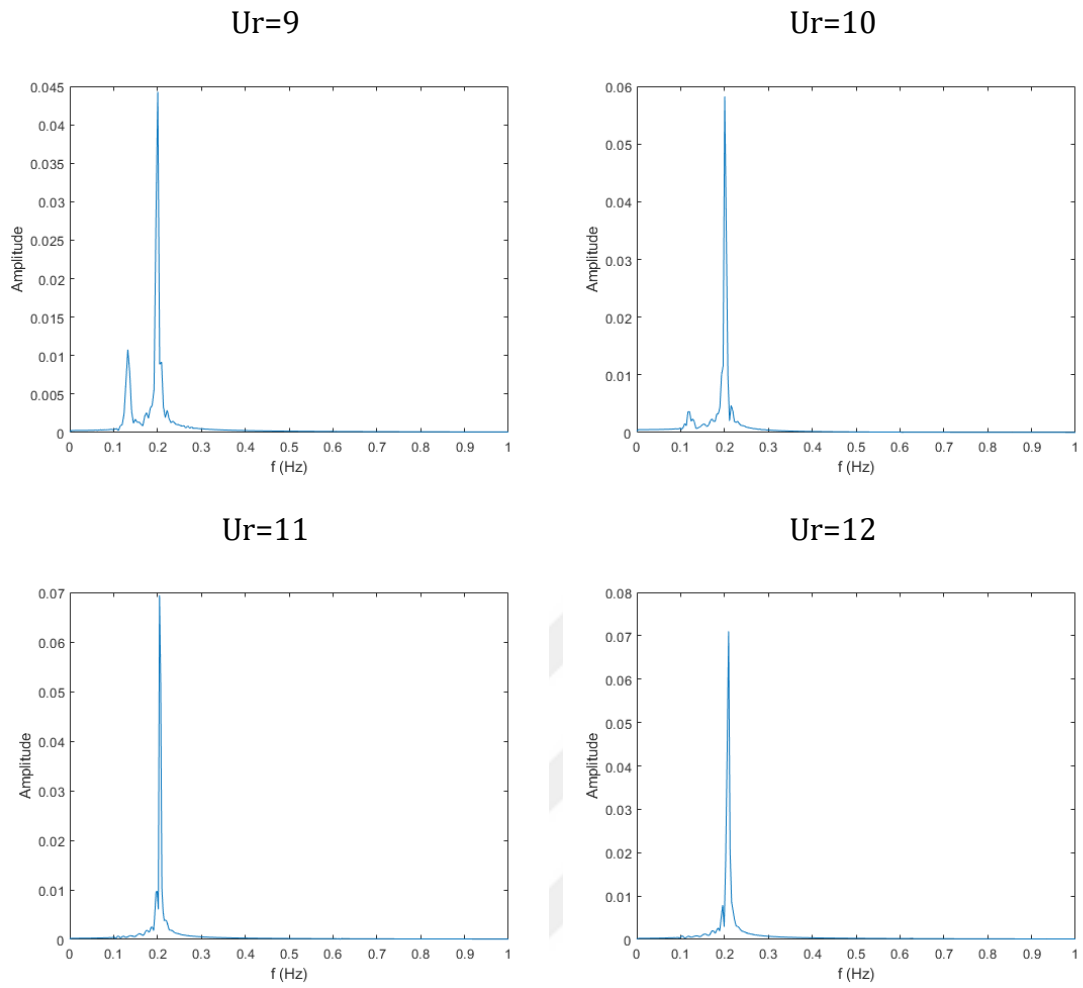


**Figure 5.9** Spectral density of displacement of corresponding  $U_r$  for  $\zeta=0.028$

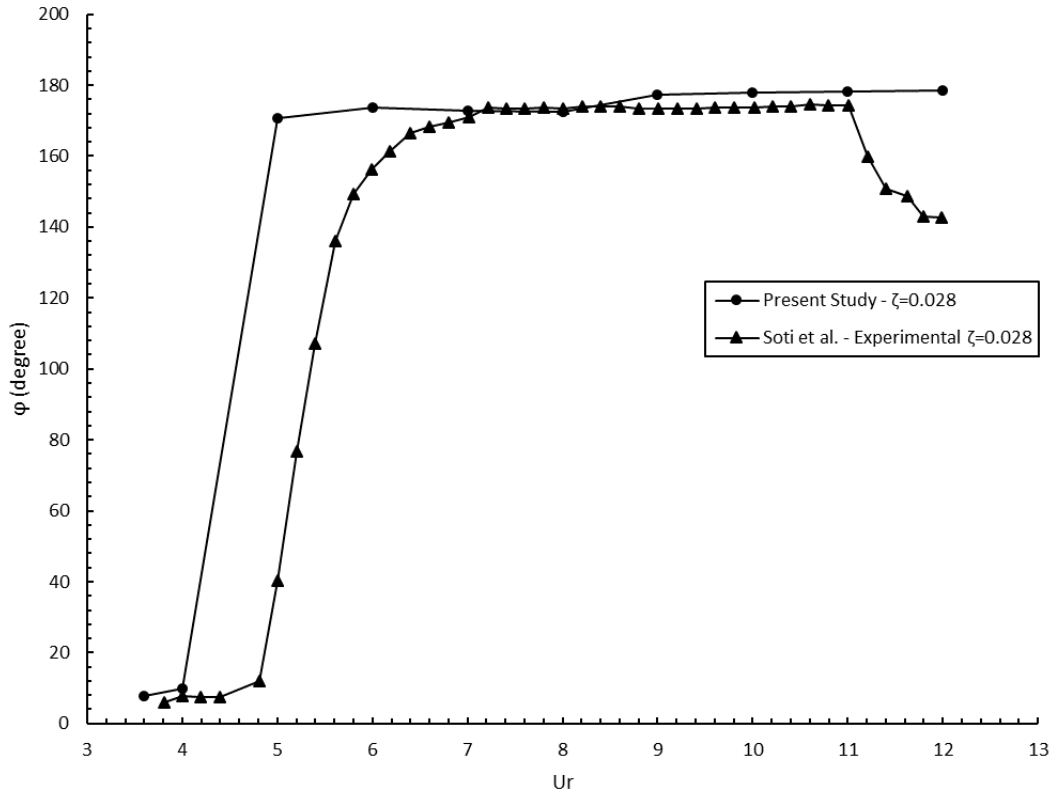


**Figure 5.10** Phase angle,  $\phi$ , as a function of corresponding  $Ur$  for  $\zeta = 0.028$

#### 5.2.4 Vortex formation modes

Figure 5.11 shows vorticity contours of corresponding  $Ur$ . Similar trend is observed as in validation simulations.  $Ur=4$  corresponds to 2S mode as an indication of initial branch. During lock-in, 2P vortex mode occurs for  $Ur=5$  and  $Ur=8$ . Again, these results are in good accordance with both numerical (Pan et al., 2007), experimental study (Govardhan and Williamson, 1999) and similar to validation.



**Figure 5.11** Vortex modes of  $Ur=4$  (2S),  $Ur=5$  (2P) and  $Ur=8$  (2P) for  $\zeta = 0.028$

### 5.3 Results for $\zeta = 0.074$

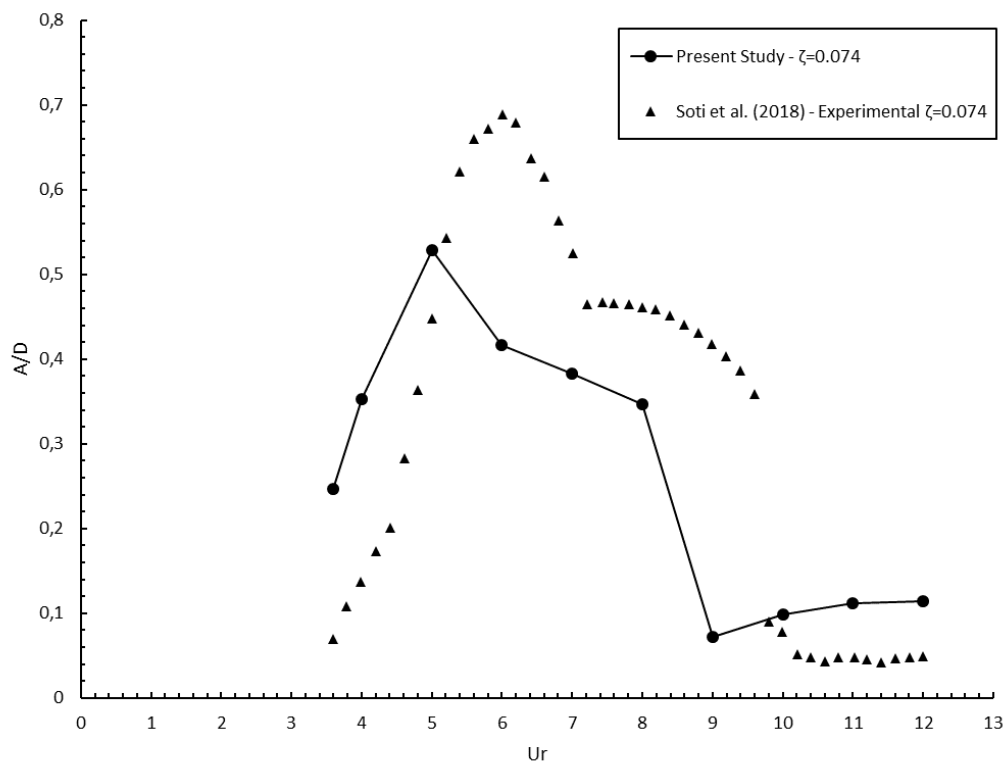
#### 5.3.1 Amplitude Ratio

Figure 5.12 shows the dimensionless amplitude ratio,  $A^*=A/D$ , as a function of corresponding reduced velocity,  $Ur$ , with comparison of experimental data (Soti et al., 2018). Both the simulations and experimental study are done with  $\zeta = 0.074$  and the mass ratio  $m^*=3$ . From the results, it can be seen that general VIV trend is captured. For  $\zeta = 0.074$ , most important result observed is there is a shift in the start of the lock-in region. For  $\zeta = 0.028$ , lock-in region starts when  $Ur=5$ . For  $\zeta = 0.074$ , lock-in region starts when  $Ur=6$  as in the experimental data by Soti et al. (Soti et al., 2018). There is an early rise in the amplitude and upper branch is not captured well

also like  $\zeta=0.028$  case due to URANS method's averaging algorithm. The highest amplitude ratio  $A^*=0.53$  is captured when  $Ur=5$  at initial branch and the highest amplitude ratio captured for the lock-in is  $A^*=0.42$  at  $Ur=6$ . From the results for both  $\zeta =0.028$  and  $\zeta =0.074$  it can be said that; the amplitude ratio decreases as the damping increase. It is expected, since the role of damping is to dissipate energy.

For  $Ur>8$  sudden decrease is observed again like for  $\zeta =0.028$  case. Also, experimental data show that desynchronization occurs early with increased damping for  $Ur>9$ .

Present work does not capture this behavior neither. These results are most likely due to the aspect ratio effect, as previously mentioned.

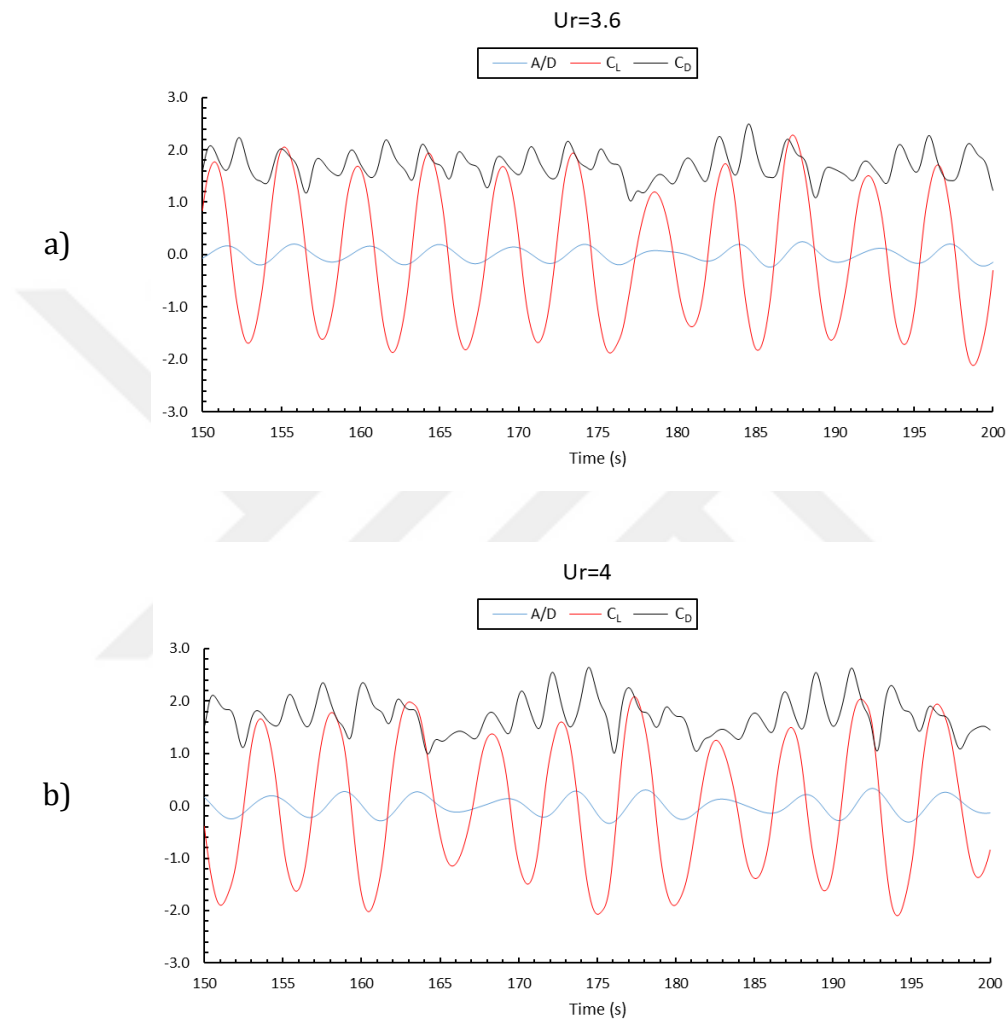


**Figure 5.12** Amplitude ratio,  $A^*$ , as a function of reduced velocity  $Ur$  for  $\zeta =0.074$

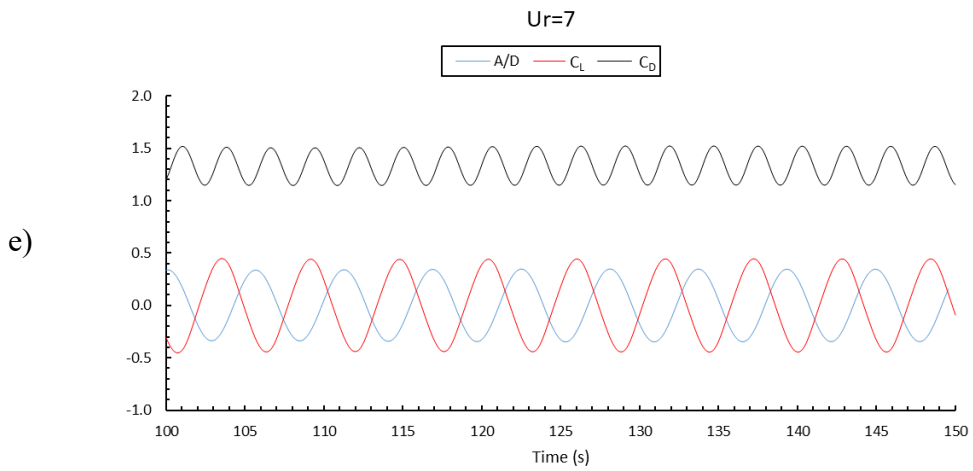
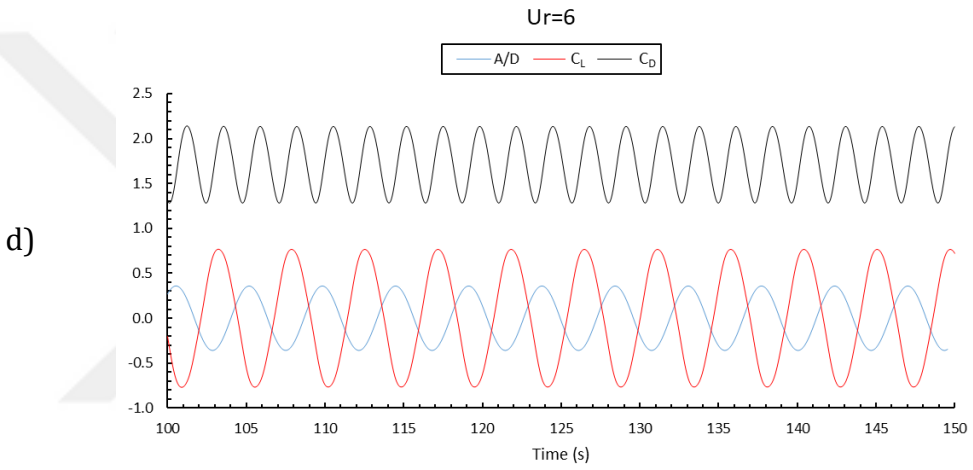
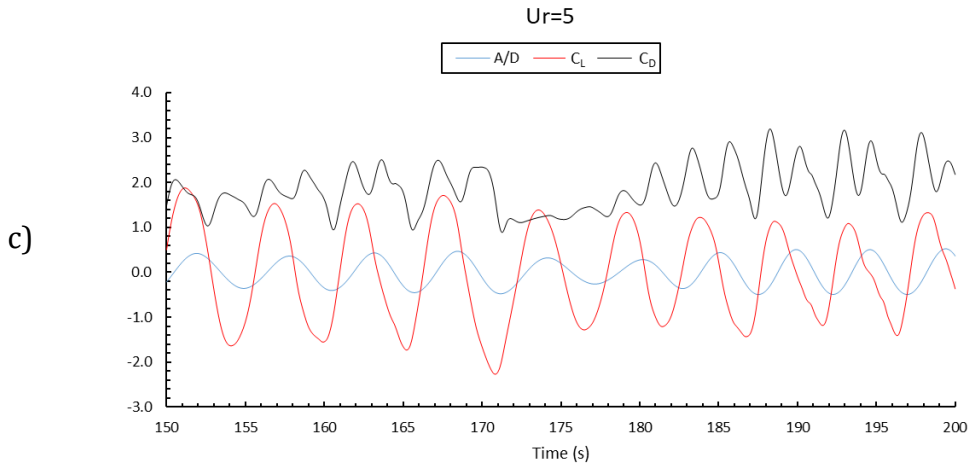
### 5.3.2 Drag and Lift Coefficients

Figure 5.13, Figure 5.14, Figure 5.15 and Figure 5.16 shows the time trace of dimensionless parameters (Dimensionless amplitude,  $A^*=A/D$ , lift coefficient,  $C_L$  and drag coefficient,  $C_D$ ). Again, the beating phenomenon at initial branch is well captured. The branch shift can be clearly seen in from the beating behavior of the time trace of  $C_L$  and  $C_D$  for  $Ur=5$ .

Similar trend is observed as lock-in starts,  $C_D$  increases dramatically in the branch transition and decreases with the increased  $U_r$ . Lift coefficient decreases in the beginning of the lock-in region and continues to decrease as the  $U_r$  increases throughout lock-in region. Contrary to the  $\zeta = 0.028$  case, for  $\zeta = 0.074$  all the  $C_L$  rms,  $C_D$  mean,  $C_L$  and  $C_D$  decrease as shown in Figure 5.17.



**Figure 5.13** Time trace of  $A^*$ ,  $C_L$  and  $C_D$  for a)  $U_r=3.6$  and b)  $U_r=4$  for  $\zeta=0.074$



**Figure 5.14** Time trace of  $A^*$ ,  $C_L$  and  $C_D$  for c)  $Ur=5$ , d)  $Ur=6$  and e)  $Ur=7$  for  $\zeta=0.074$

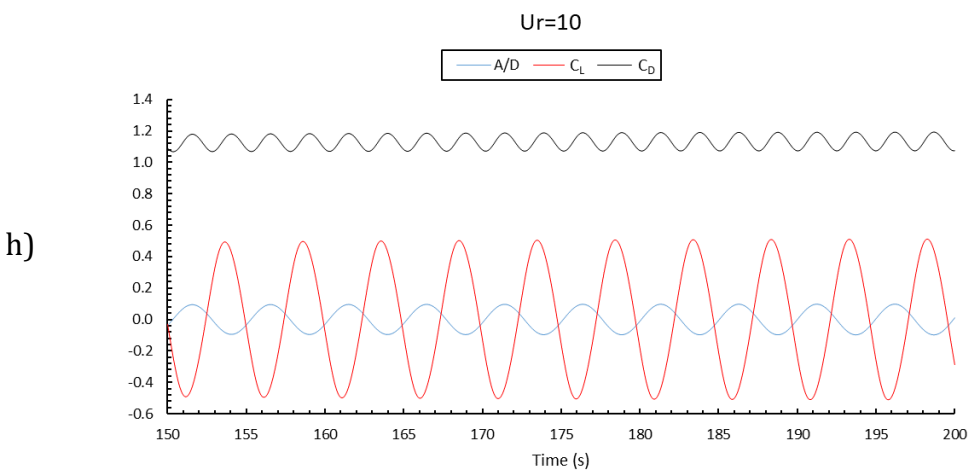
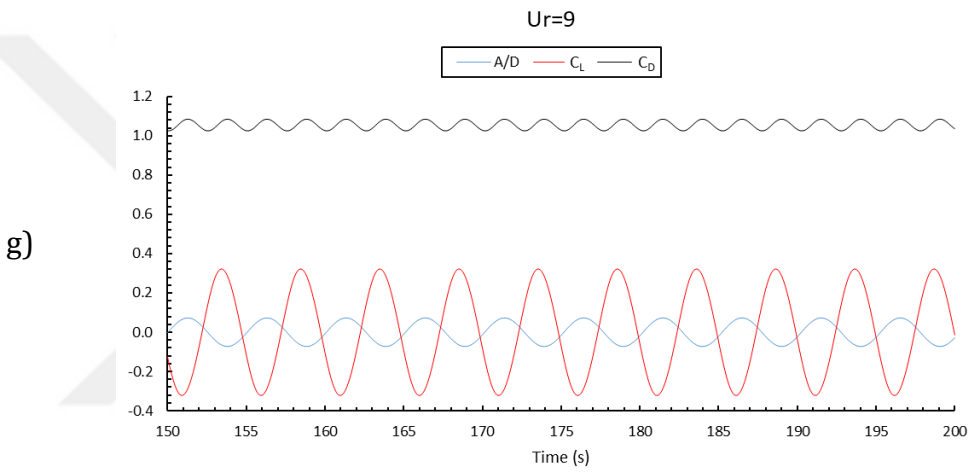
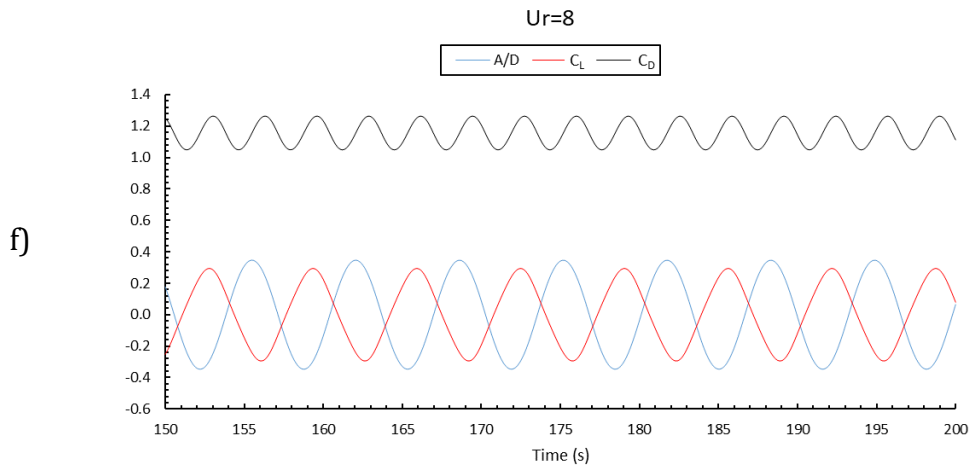


**Figure 5.15** Time trace of  $A^*$ ,  $C_L$  and  $C_D$  for f)  $Ur=8$ , g)  $Ur=9$  and h)  $Ur=10$  for

$$\zeta=0.074$$

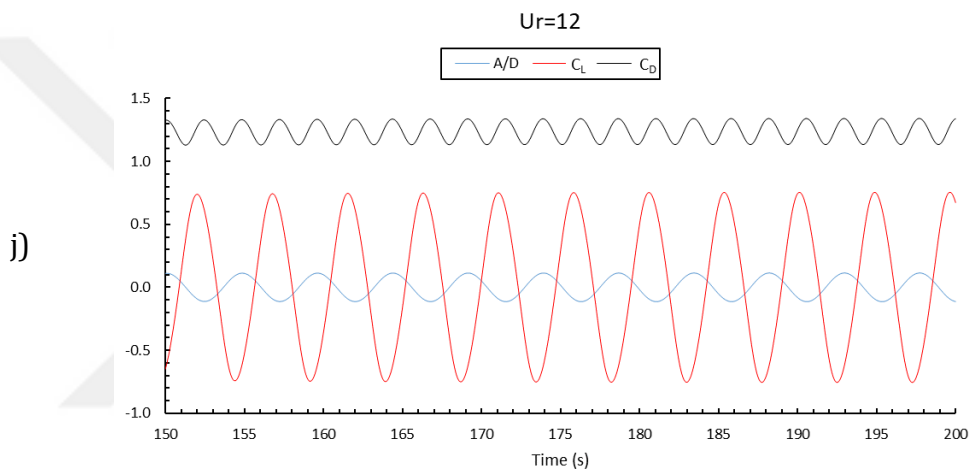
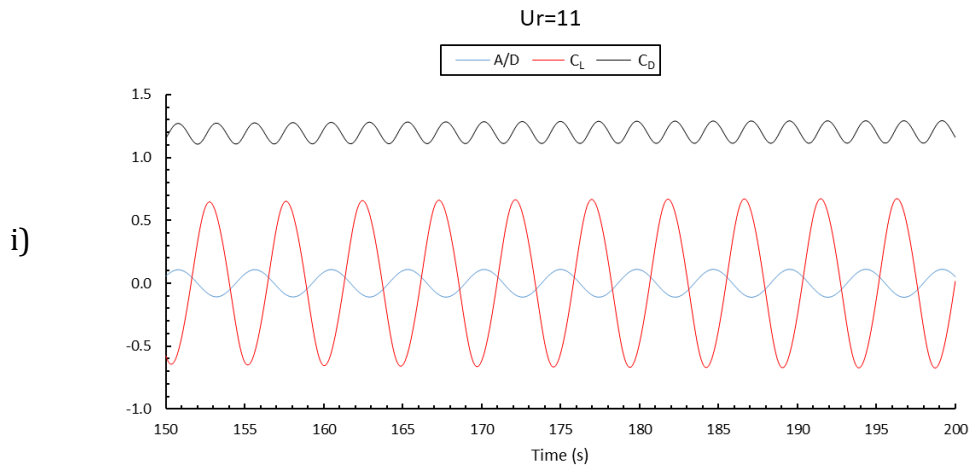


**Figure 5.16** Time trace of  $A^*$ ,  $C_L$  and  $C_D$  for i)  $Ur=11$  and j)  $Ur=12$  for  $\zeta=0.074$

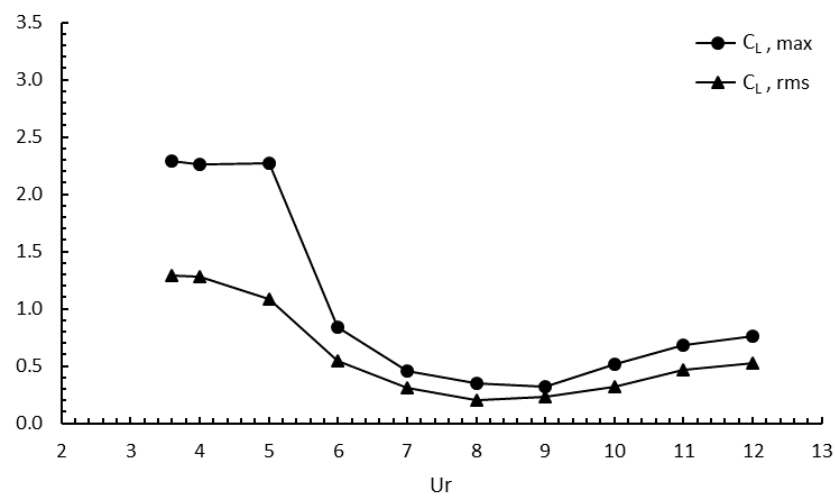
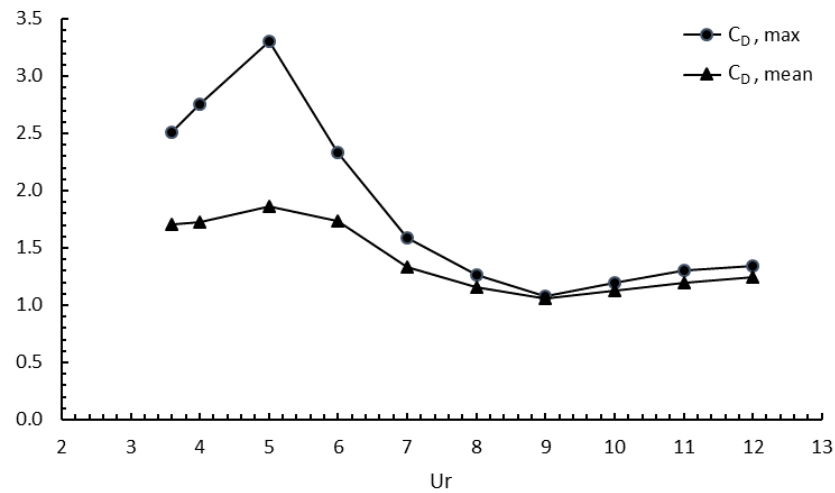


**Figure 5.17** Summary of force coefficients in terms of  $C_D$  max,  $C_D$  mean,  $C_L$  max and  $C_L$  rms as function of corresponding  $Ur$  for  $\zeta=0.074$

### 5.3.3 Frequency Ratio and Phase Angle

The frequency ratio  $f^*$  is shown in Figure 5.18 as a function of corresponding  $Ur$ . Also, the experimental spectral graph (Soti et al., 2018) is shown in the figure for  $\zeta=0.074$ . Figure 5.19 and Figure 5.20 shows the spectral density of the displacement of the cylinder for  $\zeta=0.074$ .

Similar trend is observed for  $\zeta=0.074$ , initial branch consists of two frequencies. When lock-in happens vortex shedding frequency locked with the natural frequency and only one dominant frequency is present that can be seen from Figure 5.19. The initial branch shift can be observed again in the graph for  $Ur=5$  which consist of two frequencies as an indication of initial branch.

Figure 5.18 shows, the jump in the beginning of the lock-in region is smaller with increased damping at the beginning of lock-in ( $Ur=6$ ) relative to  $\zeta =0.028$ . Like  $\zeta=0.028$  case, the upper branch is not captured well neither, so the frequency ratio in the upper branch. Similarly, initial ( $Ur<6$ ) and lower branches ( $7\leq Ur\leq 8$ ) for the present work agrees well with the experimental data. For  $Ur>8$  desynchronization is observed again.

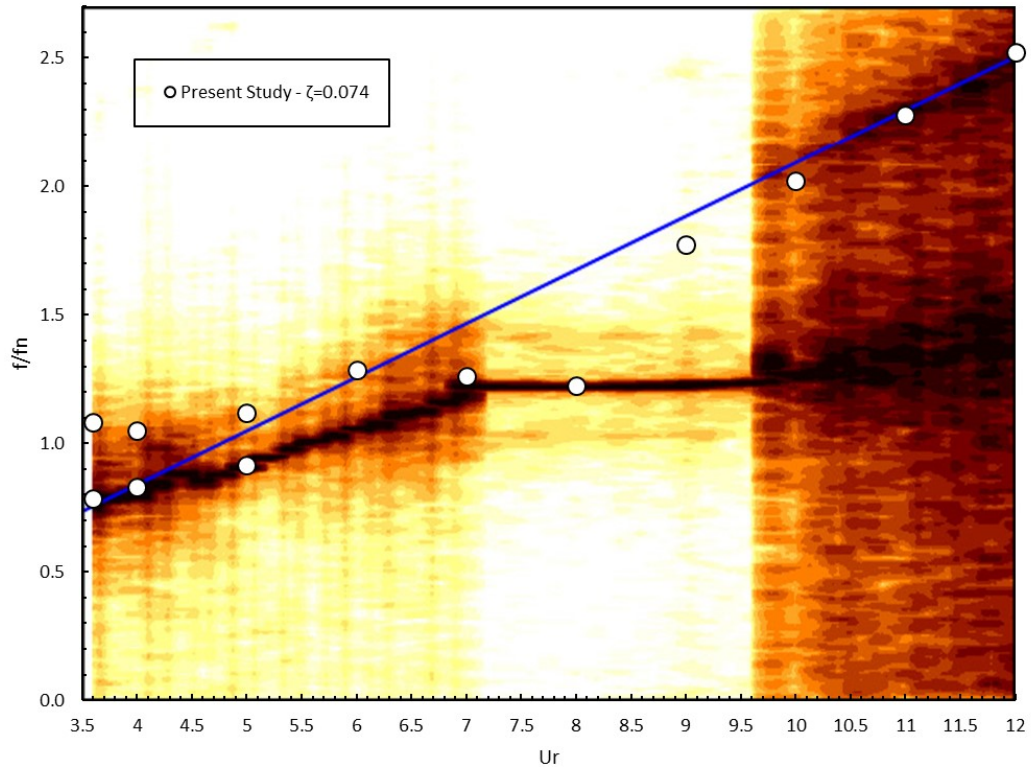


**Figure 5.18** Frequency ratio  $f^*$  as a function of corresponding  $Ur$  for  $\zeta=0.074$

The phase angle,  $\phi$ , is shown in Figure 5.21 as a function of  $Ur$  with the comparison of vortex phase of the experimental data by Soti et al. (Soti et al., 2018).

Similarly, during initial branch, the fluid forces and the displacement are in phase. Also, initial branch shift at  $Ur=5$  and the smooth transition of initial branch to lock-in region captured well contrary of  $\zeta =0.028$  case. After  $Ur=6$ , a sudden change in  $\phi$  is happened due to start of lock-in as the fluid forces and the displacement is no longer in phase. It is observed that with increased damping; the phase angle decreases during lock-in relative to the  $\zeta =0.028$  case. Overall, the initial branch and lock-in region of present study ( $3.6\leq Ur\leq 8$ ) are in good agreement with the experimental data. However, there is a difference in the desynchronization region.

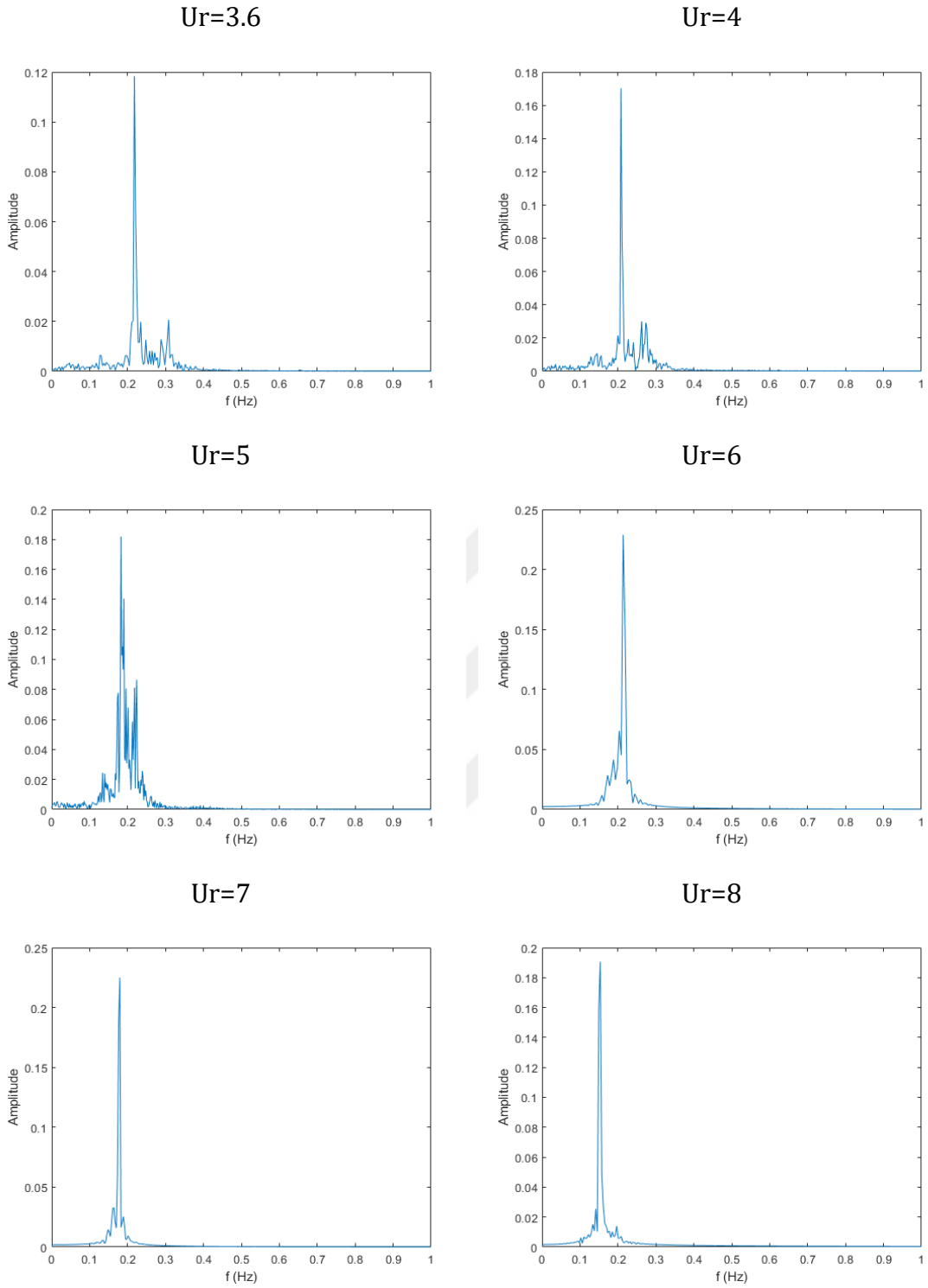


**Figure 5.19** Spectral density of displacement of corresponding  $U_r$  for  $\zeta = 0.074$

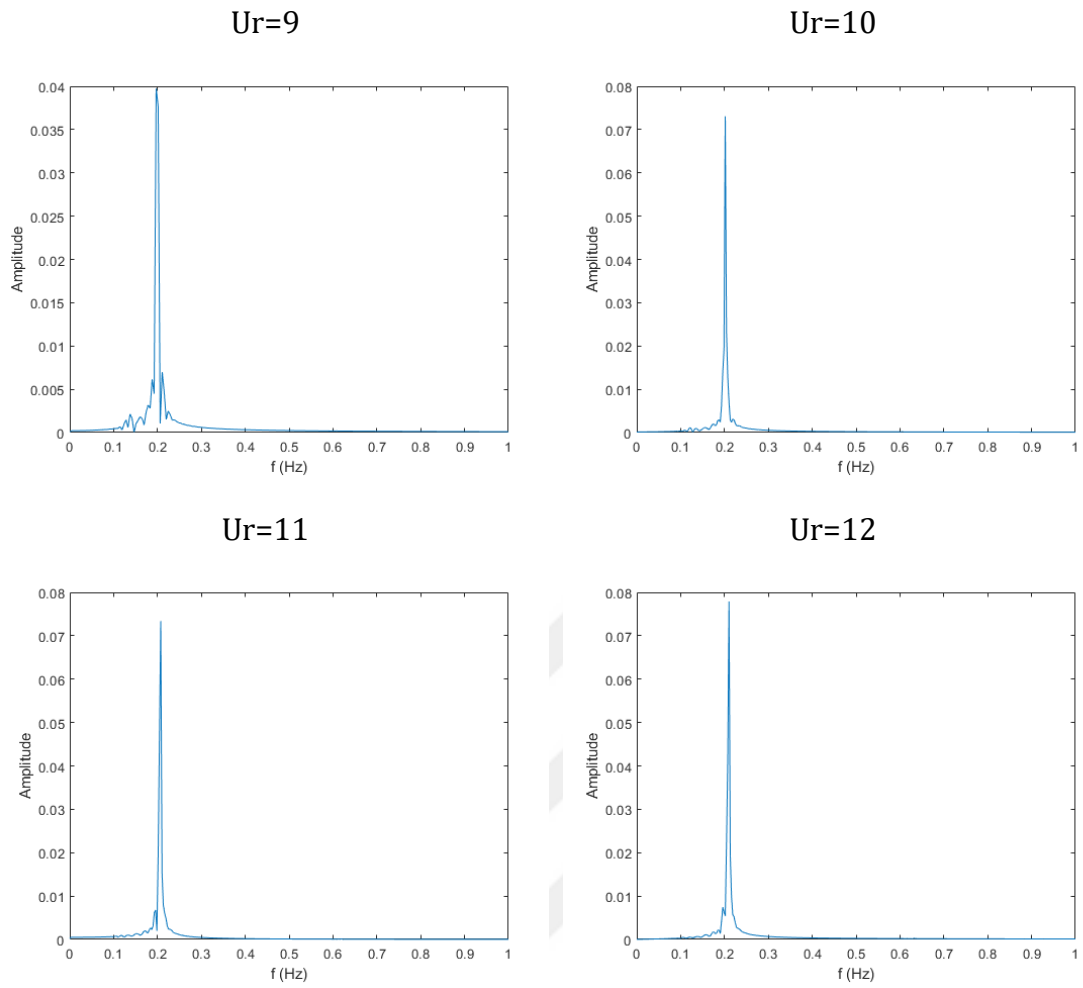


**Figure 5.20** Spectral density of displacement of corresponding  $U_r$  for  $\zeta = 0.074$

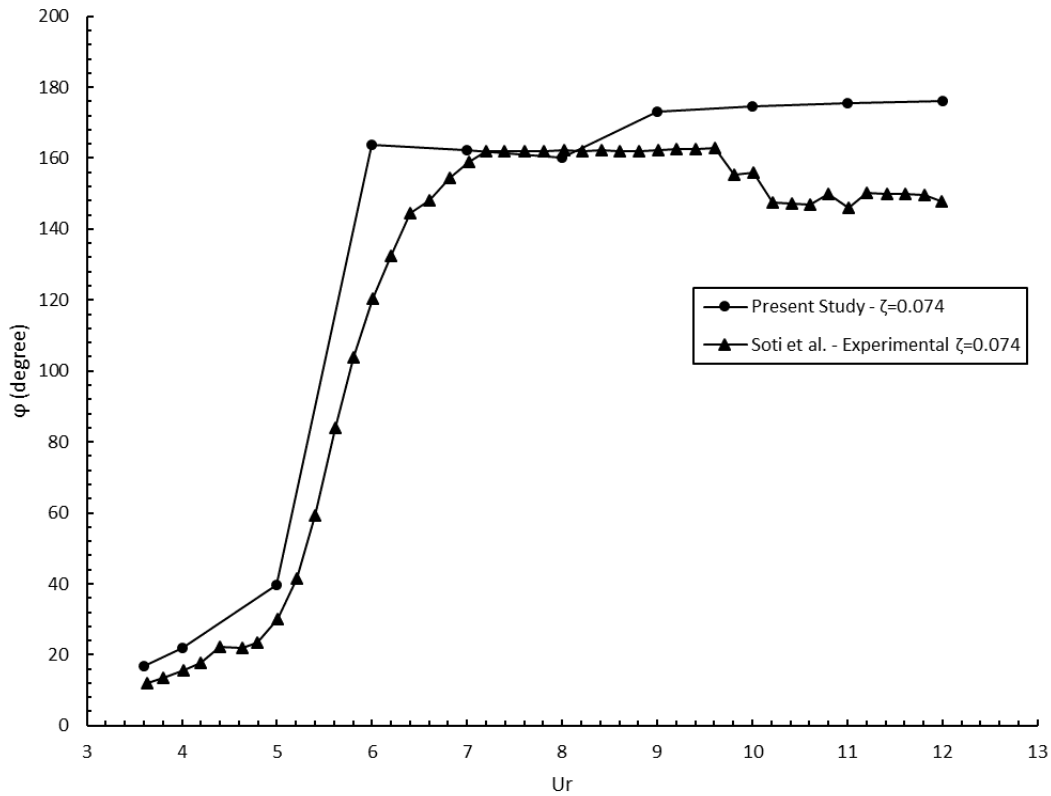


**Figure 5.21** Phase angle,  $\phi$ , as a function of corresponding  $Ur$  for  $\zeta = 0.074$

### 5.3.4 Vortex Formation Modes

Figure 5.22 shows vorticity contours of corresponding  $Ur$ . As previously mentioned, there is a shift in the initial branch. For  $Ur=5$  vortex shedding mode is 2S which is an indication of initial branch. For  $Ur \geq 6$  lock-in occurs and the vortex shedding mode changed to 2P mode. Overall, it can be said that the results are consistent with the experimental data. Again, these results are in good accordance with both numerical (Pan et al., 2007), experimental study (Govardhan and Williamson, 1999) and similar to validation.



**Figure 5.22** Vortex modes of  $Ur=5$  (2S),  $Ur=6$  (2P) and  $Ur=8$  (2P) for  $\zeta = 0.074$

### 6.1 Conclusion

In this study, 2D VIV simulations of 1DOF in the transverse direction of a cylindrical structure with different damping parameters are evaluated. The results are presented as dimensionless parameters namely; amplitude ratio, lift and drag coefficients, frequency ratio and phase angle. Also, vortex shedding modes are shown. Overall, the general trend is well captured, especially for initial and lower branches, however due to 2D limitations some results are not consistent with experimental data.

As a summary;

- With increased damping amplitude ratio, lift and drag coefficient decrease.
- The increase in damping causes a delay in transition to lock-in region.
- Due to limitations of 2D domain, amplitude ratio is lower than the experimental data and the lock-in region is narrower. This is expected, since previous study by Rahman and Thiagarajan (2015) shows similar effect of aspect ratio.
- Upper branch is not captured well for both cases. This is also reported by both Guilmineau and Queutey (2004) and Pan et al. (2007).
- Phase angle is decrease as the damping increases during lock-in.

### 6.2 Future work suggestions

As a future work;

- 3D domain VIV simulations with different damping parameters should be studied and compared the results with experimental data to evaluate the aspect ratio effect.

- 2D domain of 2DOF VIV simulations with different damping parameters should be studied to investigate the VIV behavior in both transverse and in-line direction.
- 1DOF VIV with several damping parameters should be studied to investigate further effect of damping.
- Different turbulence model (i.e. RSM,  $k-\epsilon$ ) should be investigated to compare results between different models.
- To better investigate the transition between branches, more reduced velocities should be studied.



```
#include "udf.h"

DEFINE_SDOF_PROPERTIES(cylinder,prop,dt,time,dttime)
{
    real cg;

    real v;

    real k = xxxx; %stiffness
    real c = xxxx; %damping
    cg = DT_CG(dt)[1];
    v = DT_VEL_CG(dt)[1];
    prop[SDOF_MASS] = 1;
    prop[SDOF_LOAD_F_Y] = (-k*cg)-(v*c);
    prop[SDOF_ZERO_TRANS_X] = TRUE;
    prop[SDOF_ZERO_TRANS_Z] = TRUE;
    prop[SDOF_ZERO_ROT_X] = TRUE;
    prop[SDOF_ZERO_ROT_Y] = TRUE;
    prop[SDOF_ZERO_ROT_Z] = TRUE;
}
```

## References

---

- Anderson, J. D. (1995). *Computational Fluid Dynamics, The basics with applications*. McGraw-Hill.
- ANSYS 2019. *ANSYS Fluent Theory Guide*, Release 2019.
- Bearman, P. W. (2009). Understanding and predicting vortex-induced vibrations. *Journal of Fluid Mechanics*, 634, 1.
- Bearman, P. W. (2011). Circular cylinder wakes and vortex-induced vibrations. *Journal of Fluids and Structures*, 27(5–6), 648–658.
- Blackburn, H. M., & Karniadakis, G. E. (1993). Two- and three-dimensional simulations of vortex-induced vibration of a circular cylinder. In: *Proceedings of the 3rd International Offshore and Polar Engineering Conference*, Vol. 3, Singapore, pp. 715–720.
- Evangelinos, C. (1999). *Parallel simulations of vortex-induced vibrations in turbulent flow: linear and non-linear models*. Ph.D. Thesis, Brown University, USA.
- Feng, C. C. (1968). *The measurements of the vortex induced effects in flow past stationary and oscillating circular and D-section cylinders*. Thesis, The University of British Columbia.
- Gopalkrishnan R. (1993). *Vortex-induced forces on oscillating bluff cylinders*. DTIC Document.
- Govardhan, R., & Williamson, C. (2000). Modes of vortex formation and frequency response of a freely vibrating cylinder. *Journal of Fluid Mechanics*, 420, 85-130.
- Govardhan, R., & Williamson, C. (2006). Defining the ‘modified Griffin plot’ in vortex-induced vibration: Revealing the effect of Reynolds number using controlled damping. *Journal of Fluid Mechanics*, 561, 147-180.
- Guilmineau, E., & Queutey, P. (2004). Numerical simulation of vortex-induced vibration of a circular cylinder with low mass-damping in a turbulent flow. *Journal of Fluids and Structures*, 19(4), 449–466.
- Hover, F., Miller, S. & Triantafyllou, M. (1997). Vortex-induced vibration of marine cables: experiments using force feedback. *J Fluid Struct*, 11(3), 307–326.
- Jauvtis, N., & Williamson, C. (2004). The effect of two degrees of freedom on vortex-induced vibration at low mass and damping. *Journal of Fluid Mechanics*, 509, 23-62.
- Kajishima, T. & Taira, K. (2017). *Computational Fluid Dynamics, Incompressible Turbulent Flows*. Springer.

- Kang, Z., Ni, W., & Sun, L. (2017). A numerical investigation on capturing the maximum transverse amplitude in vortex induced vibration for low mass ratio. *Marine Structures*, 52, 94–107.
- Khalak, A., & Williamson, C. H. K. (1996). Dynamics of a hydroelastic cylinder with very low mass and damping. *Journal of Fluids and Structures*, 10(5), 455–472.
- Khalak, A., & Williamson, C. H. K. (1997). Fluid forces and dynamics of a hydroelastic structure with very low mass and damping. *Journal of Fluids and Structures*, 11(8), 973–982.
- Khalak, A., & Williamson, C. H. K. (1999). Motions, forces and mode transitions in vortex-induced vibrations at low mas-damping. *Journal of Fluids and Structures*, 13(7–8), 813–851.
- Khan, N. B., & Ibrahim, Z. (2018). Numerical investigation of vortex-induced vibration of an elastically mounted circular cylinder with One-degree of freedom at high Reynolds number using different turbulent models. *Proceedings of the Institution of Mechanical Engineers, Part M: Journal of Engineering for the Maritime Environment*, 233(2), 443–453.
- Klamo, J. T., Leonard, A., & Roshko, A. (2005). On the maximum amplitude for a freely vibrating cylinder in cross-flow. *Journal of Fluids and Structures*, 21(4), 429–434.
- Klamo, J. T., Leonard, A., & Roshko, A. (2006). The effects of damping on the amplitude and frequency response of a freely vibrating cylinder in cross-flow. *Journal of Fluids and Structures*, 22(6–7), 845–856.
- Li, W., Li, J., & Liu, S. (2014). Numerical simulation of vortex-induced vibration of a circular cylinder at low mass and damping with different turbulent models. *OCEANS 2014 - TAIPEI, Taipei*, pp. 1-7.
- Menter, F. R. (1994). Two-equation eddy-viscosity turbulence models for engineering applications. *AIAA J* 1994; 32(8): 1598–1605.
- Morse, T. L. (2009). Fluid forcing, wake modes, and transitions for a cylinder undergoing controlled oscillations. *Journal of Fluids and Structures*, 25(4), 697–712.
- Newman, D. J., & Karniadakis, G. E. (1997). A direct numerical simulation study of flow past a freely vibrating cable. *Journal of Fluids Mechanics* 344, 95–136.
- Nguyen, V-T & Nguyen, H. H. (2016). Detached eddy simulations of flow induced vibrations of circular cylinders at high Reynolds numbers. *J Fluid Struct*, 63, 103–119.
- Norberg C. (2003). Fluctuating lift on a circular cylinder: review and new measurements. *Journal of Fluids and Structures*, 17(1), 57–96.
- Pan, Z. Y., Cui, W. C., & Miao, Q. M. (2007). Numerical simulation of vortex-induced vibration of a circular cylinder at low mass-damping using RANS code. *Journal of Fluids and Structures*, 23(1), 23–37.
- Rahman, M. A. A., & Thiagarajan, K. P. (2015). Experiments on vortex-induced vibration of a vertical cylindrical structure: Effect of low aspect

ratio. *International Journal of Automotive and Mechanical Engineering*, 11(1), 2515-2530.

- Saltara, F., Meneghini, J. R., & Siquiera, C. L. R. (1998). The simulation of vortex shedding from an oscillating circular cylinder. In: *Proceedings of the 8th International Offshore and Polar Engineering Conference*, Vol. 3, Montreal, Canada, pp. 356–363.
- Sarpkaya, T. (2004). A critical review of the intrinsic nature of vortex-induced vibrations. *Journal of Fluids and Structures*, 19(4), 389–447.
- Soti, A. K., Zhao, J., Thompson, M. C., Sheridan, J., & Bhardwaj, R. (2018). Damping effects on vortex-induced vibration of a circular cylinder and implications for power extraction. *Journal of Fluids and Structures*, 81, 289–308.
- Sumer, B. M., & Fredsøe, J. (1997). *Hydrodynamics Around Cylindrical Structures* (Vol. 12). Singapore: World Scientific.
- Willcox, D. C. (1988). *Turbulence Modeling for CFD*. DWC Industries, Inc., La Canada, California.
- Williamson, C. H. K., & Govardhan, R. (2004). Vortex-induced vibrations. *Annual Review of Fluid Mechanics*. 36, 413–455.
- Williamson, C. H. K., & Roshko, A. (1988). Vortex formation in the wake of an oscillating cylinder. *Journal of Fluids and Structures*, 2(4), 355–381.

## **Publications from the thesis**

---

**Contact Information:** f5215015@std.yildiz.edu.tr

### **Conference Paper**

Mutlu, A. O, Bayraktar, M. & Bayraktar, S. (2019). 1DOF 2D URANS simulation of vortex-induced vibration of a cylinder with different damping parameters. 4th International Congress on Engineering, Architecture and Design. Congress Book, 4, Istanbul, Turkey, 930-937.

